Intraseasonal Variability of Anticyclonic Rossby Wave Breaking and Its Impact on Tropical Cyclone Activity over the Western North Pacific

YITIAN QIAN,[a] PANG-CHI HSU,[a] HIROYUKI MURAKAMI,[b] GAN ZHANG,[c] HUIJUN WANG,[a] AND MINGKENG DUAN[a]

[a] *Key Laboratory of Meteorological Disaster, Ministry of Education (KLME), Collaborative Innovation Center on Forecast and Evaluation of Meteorological Disasters (CIC-FEMD), Joint International Research Laboratory of Climate and Environment Change (ILCEC), Nanjing University of Information Science and Technology, Nanjing, China*
[b] *Geophysical Fluid Dynamics Laboratory, Princeton, New Jersey*
[c] *Department of Atmospheric Sciences, University of Illinois Urbana–Champaign, Urbana, Illinois*

(Manuscript received 17 February 2023, in final form 7 October 2023, accepted 17 October 2023)

ABSTRACT: The intraseasonal variations in anticyclonic Rossby wave breaking (AWB) events, which are characterized by synoptic-scale irreversible meridional overturning of potential vorticity over the North Pacific, and their modulations on tropical cyclone (TC) activity over the western North Pacific (WNP), were investigated in this study. Spectral analysis of the AWB frequency shows significant variability within a period of 7–40 days, closely linked to the subseasonal variability of the jet stream intensity. When the jet stream weakens at its exit region over the North Pacific, the AWB occurs along with an equatorward Rossby wave flux. This AWB is preceded by an intensified Rossby wave train across Eurasia 12 days earlier. Simultaneously, a high potential vorticity intrusion is advected in the upper troposphere from the North Pacific toward the WNP, and suppressed TC activities are observed over the WNP open ocean where decreased moisture and temperature, subsidence, and increased vertical wind shear prevail. In contrast, anomalously enhanced convection, positive relative vorticity, and ascending motion are found in the southwestern quadrant of the AWB, facilitating enhanced TC activities over the South China Sea (SCS). Further analysis indicates that the impact of the AWB on TC activities over the WNP is robust and independent of the tropical intraseasonal convection over the tropical Indian Ocean and SCS, even though it accompanies the increased AWB frequency.

KEYWORDS: North Pacific Ocean; Rossby waves; Tropical cyclones; Intraseasonal variability

1. Introduction

Rossby wave breaking (RWB) occurs when the vorticity gradient of the environmental flow cannot support the linear propagation of Rossby waves. During RWB, the flow field deforms nonlinearly and irreversibly, resulting in strong mixing of air masses across latitudes (Waugh et al. 1994; Waugh and Polvani 2000). The RWB process is often characterized by the meridional overturning of potential vorticity (PV) contours on the isentropic surface (McIntyre and Palmer 1983; Appenzeller and Davies 1992). Regulated by seasonal variations of the large-scale circulation, the frequency and location of RWB have a significant seasonal cycle (e.g., Abatzoglou and Magnusdottir 2006; Wernli and Sprenger 2007). Throughout the year, RWB activities are closely related to extratropical variability and often facilitate extreme weather events.

Two types of RWBs have been identified based on PV streamer patterns (Thorncroft et al. 1993). One is the anticyclonic RWB (AWB) that occurs in an anticyclonically sheared environment over the equatorward flank of the jet stream, wherein the high-PV streamers extend equatorward under low-PV air. The other is the cyclonic RWB (CWB) with cyclonically sheared PV streamers that occur in the poleward region of the climatological jet [see the schematic (Fig. 13) in Thorncroft et al. (1993)]. Both types of RWBs demonstrate two-way interactions with the midlatitude jet stream. A poleward (equatorward) shift of the jet favors more AWB (CWB) occurrence (Rivière et al. 2010), which in turn displaces the original jet further poleward (equatorward) through momentum transfer (Thorncroft et al. 1993; Rivière et al. 2010). The two types of RWB have distinct signatures in eddy energetics (Thorncroft et al. 1993) and material transport (Thorncroft et al. 1993; Polvani and Esler 2007).

During the winter, RWB is an important contributor to the variability and the extremes of extratropical circulation. AWB (CWB) is associated with a positive (negative) North Atlantic Oscillation phase through its influence on local momentum fluxes (Benedict et al. 2004; Abatzoglou and Magnusdottir 2006; Strong and Magnusdottir 2008; Woollings et al. 2008). Similar modulations of AWB (CWB) on the positive (negative) phase of the Northern Hemisphere Annular Mode and Pacific–North American teleconnection pattern via jet positioning shifts have also been identified (Franzke et al. 2011). In addition, RWB activities influence the occurrence of cold temperatures in East Asia (Song and Wu 2021), European windstorms (Messori and Caballero 2015), landfalling atmospheric river events along the U.S. West Coast (Hu et al. 2017), extreme precipitation in the central and eastern United States (Moore et al. 2019), and the tropical water cycle (Aemisegger et al. 2021). During boreal summer, AWB occurrences increase in the subtropics owing to relatively weak and poleward shifted midlatitude jet streams. Takemura and Mukougawa (2020a,b) revealed the significant role of AWB in a process linking the quasi-stationary Rossby wave propagation along the jet and the Pacific–Japan teleconnection pattern. Based on an analysis of 44 AWB events (hereinafter, "AWBs") to the east of Japan,

Corresponding author: Pang-Chi Hsu, pangchi@nuist.edu.cn

DOI: 10.1175/JCLI-D-23-0091.1

Takemura and Mukougawa (2020a,b) identified a significant role of AWB in inducing the Pacific–Japan teleconnection pattern. When AWB occurs, the upper-level positive vorticity advection associated with it can induce upward motion and strengthening of the tropical convection over the subtropical western North Pacific (WNP) and then excite the Pacific–Japan pattern dynamically. Enhanced AWB frequency is significantly related to a stronger preceding quasi-stationary Rossby wave train and a subsequently enhanced Pacific–Japan pattern (Takemura and Mukougawa 2020a,b). The interannual variability of RWB frequency near Japan increases significantly during La Niña years (Takemura et al. 2020). AWBs could lead to dry episodes of the Indian summer monsoon by transporting high-PV air equatorward (Samanta et al. 2016).

The maximum occurrence centers of AWB in boreal summer are over the subtropical North Pacific and North Atlantic, located more westward than their winter counterparts (Abatzoglou and Magnusdottir 2006; Bowley et al. 2019) and adjacent to tropical cyclone (TC) tracks (Wang et al. 2020). AWB variability has recently been recognized as an important extratropical signal in modulating TC activities over the North Atlantic (Li et al. 2018; Zhang et al. 2016, 2017). The AWB activity induces a stronger vertical wind shear (VWS) as well as a drier and colder tropospheric atmosphere over the Atlantic main development region, consistently reducing TC genesis counts as well as their lifetimes, intensities, and landfalls over the North Atlantic. Zhang et al. (2017) suggested that this extratropical impact induced by AWBs may be comparable to the impact by warming tropical SST forcings, as demonstrated in the SSTs of the Atlantic Ocean's main TC development region and the Niño-3.4 index. Li et al. (2018) also found a similar impact of the AWB variability on TC activities over the North Atlantic at subseasonal time scales. At least part of the RWB variability can be predicted on the subseasonal-to-seasonal scale (Zavadoff and Kirtman 2021; Zhang et al. 2021; Jones et al. 2022). Moreover, the increased AWB frequency was found to result in lower TC prediction skill in the Global Ensemble Forecasting System (Li et al. 2018) and Navy Earth System Prediction Capability (Papin et al. 2023).

The WNP is the most active region for TC generation in the world. Because the RWB frequency over the North Pacific is more frequent than that over the North Atlantic in summer (Abatzoglou and Magnusdottir 2006; Bowley et al. 2019), some studies have noted the impact of AWBs on TC activities over the WNP. Bian et al. (2018) found that the absence of WNP TC generation in August 2014 resulted from the joint influence of a suppressed phase of the tropical Madden–Julian oscillation (MJO) and anomalously active AWBs. The irreversible PV streamers associated with the increased AWB frequency brought cold and dry air from the extratropics to the tropics and thus restrained the TC activity in August 2014. Zhang et al. (2016, 2017) also made a similar conclusion regarding the influence of AWBs on TCs in the North Atlantic. Recently, Takemura and Mukougawa (2021) found that the anomalous low-level convergence and enhanced convection that occurs in the southwestern quadrant of AWBs favor TC activity there, based on a climatological composite approach. The strength and location of the tropical upper-tropospheric trough are closely related to RWB activities and could modulate TC activities significantly over the tropical North Pacific (Wu et al. 2015; Wang and Wu 2016; Feng and Wu 2022) and North Atlantic (Wang et al. 2020) at interannual to interdecadal time scales.

To date, little is known about the influence of AWBs on WNP TC activities at intraseasonal time scales. A limited understanding of potential sources of subseasonal TC predictability is one of the main reasons for the low skill of TC prediction at subseasonal time scales (Camargo et al. 2019; Lee et al. 2020; Qian et al. 2020). Thus, we aim to address the following questions in this study: 1) What are the features of AWB variability and its associated large-scale anomalies over the WNP during the TC season (June–November) at subseasonal time scales? 2) How—and to what extent—do the intraseasonal AWB variations affect TC activities over the WNP?

The rest of the paper is organized as follows: data and methods employed are introduced in section 2. The basic characteristics of AWBs and their associated large-scale anomalies at subseasonal time scales over the WNP are presented in section 3. In section 4, we quantify the intraseasonal modulation of AWBs on WNP TC activities and identify the key processes accounting for the AWB–TC connection. The discussion and conclusions are presented in section 5.

2. Data and methods

a. Data

1) Large-scale field datasets

RWB frequency is identified based on the daily PV at 350-K isentropic levels from the state-of-the-art ECMWF reanalysis dataset, ERA5 (Hersbach et al. 2020). To analyze the large-scale fields associated with the intraseasonal variability of AWB over the WNP, the daily zonal and meridional wind (u and v), vertical p velocity (ω), temperature (T), geopotential height (Z), and specific humidity (q) at 21 vertical pressure levels from 1000 to 100 hPa with a horizontal resolution of 1° × 1° from ERA5 are utilized. The daily variables are averaged from the 0000, 0600, 1200, and 1800 UTC data. Considering that this study focuses on the intraseasonal variations of AWBs and TC activities, which both display a large-scale feature geographically, we utilize the ERA5 data at the resolution of 1°. These 1° × 1° data were obtained directly from the ERA5 server and derived from the bilinear interpolation method (Hersbach et al. 2018). VWS is defined as follows: $\mathrm{VWS} = \sqrt{(\mathrm{u200} - \mathrm{u850})^2 + (\mathrm{v200} - \mathrm{v850})^2}$. The u200 (v200) and u850 (v850) represent the zonal (meridional) wind speed at 200 and 850 hPa, respectively. We use daily outgoing longwave radiation (OLR) data at a horizontal resolution of 2.5° × 2.5° from the polar-orbiting satellites of the National Oceanic and Atmospheric Administration (Liebmann and Smith 1996) to identify deep convection activity. These data cover the WNP TC season (June–November) during 1979–2020.

2) TC datasets

To ensure the robustness of results, two TC best track datasets are utilized. One is the U.S. Department of Defense Joint

Typhoon Warning Center (JTWC) Best Track Database, and the other is from the Regional Specialized Meteorological Center (RSMC) Tokyo–Typhoon Center. Both datasets include the TC latitude, longitude, and maximum wind speed every 6 h over the WNP (0°–60°N, 90°E–180°). JTWC uses a 1-min average sustained 10-m wind speed for the maximum wind speed, while RSMC uses a 10-min average value. Since the 10-min average wind speed is approximately 88% of the 1-min average wind speed (Atkinson 1974), the maximum wind speed from RSMC is divided by 0.88 to convert it to a 1-min average wind speed, making it comparable to that from JTWC under the same criterion. We focus on TCs with tropical storm intensity or higher (wind speed ≥ 17 m s^{-1}) in this study.

b. Methods

1) Detection of RWB

Following the detection algorithm described in Abatzoglou and Magnusdottir (2006) and Strong and Magnusdottir (2008), we detect RWB events by searching for high-PV tongues associated with the overturning of PV contours on the 350-K isentropic surface. We focus on the longest circumpolar PV contours with PV values of 1.5–7.0 PV units (1 PVU = 10^{-6} K kg^{-1} m^2 s^{-1}). Then, the PV overturning associated with the RWB is identified by finding the PV contours with the longest circumpolar contour crossing a meridian more than once. The detected overturning is counted as one RWB event. The AWB (CWB) is determined when the latitude of the first point of intersection is higher (lower) than that of the last point of intersection when we search eastward along the PV contours. In this study, we focus only on AWBs. For each AWB event, the location of the AWB is defined as the centroid of the equatorward tongue of the high-PV air region. More details of the AWB detection algorithm can be found in Abatzoglou and Magnusdottir (2006) and Strong and Magnusdottir (2008). Following previous studies (Zhang et al. 2016, 2017; Li et al. 2018), we count the AWBs in 5° × 5° grid boxes to define the spatial distribution of the AWB frequency. The spatial pattern of AWBs is not sensitive to the sizes of the box for statistical analysis. The results of the climatological mean and standard deviation of AWB frequency derived from different box sizes (not shown) are consistent. They also remain similar to those observed in 5° × 5° grid cells, with the maximum frequency center in the central North Pacific over the equatorward sector of the westerly jet exit.

To focus closely on the intraseasonal components of AWB variability, we remove the high-frequency synoptic signals of AWB by applying a temporal smoothing (5-day running mean) to the time series of AWBs. The intraseasonal components of AWB-related fields illustrated in section 2a(1) are also obtained by first removing the annual cycle (the mean and first three harmonics of the daily climatology). Then, a 5-day running mean is applied to remove the synoptic-scale variability. Although the time filtering may introduce temporal dependency in time series data, it does not affect the qualitative discussion of the evolving features. This holds particularly true when we focus on the subseasonal variability. The partial overlap of daily data (e.g., using data from days −4 to 0 for day −2, and from days −2 to +2 for day 0) does not alter the overall tendency but instead illustrates its smoother changes.

2) Statistical analysis of TC activities

To elucidate the ways in which AWB influences TC activities at subseasonal time scales, several metrics representing TC activities are used, including the TC genesis count, TC frequency, and accumulated cyclone energy (ACE; Bell et al. 2000) over a 10-day period. For each 5° × 5° grid cell during the tth 10-day period in a TC season, the TC genesis number is counted when the TC surface maximum wind speed exceeds 17 m s^{-1} for the first time in each grid cell, and the TC frequency is the total frequency of TC occurrences in a grid cell. ACE is a measure that quantifies the cumulative impact of TC activities, which is calculated by summing the square of the maximum wind speed of the TC recorded every 6 h in a certain grid cell, as follows:

$$\mathrm{ACE} = \sum_{k=1}^{\mathrm{Freq}} V_{\max}^2(k), \tag{1}$$

in which $V_{\max}(k)$ refers to the maximum wind speed recorded in the kth 6-h record and "Freq" indicates the frequency of TC occurrence in the grid cell.

ACE incorporates the influential factors of TC count N, duration D, and intensity I. To examine the relative contributions of these factors to ACE changes, we applied the ACE decomposition method proposed by Drews (2007) in each 10-day epoch, as follows:

$$\mathrm{ACE} = N\frac{\mathrm{Freq}}{N}\frac{\sum_{k=1}^{\mathrm{Freq}} V_{\max}^2(k)}{\mathrm{Freq}} = N \times D \times I. \tag{2}$$

Here, N represents the number of TC cases that occur in a certain grid cell. For instance, if a named TC occurs in a certain grid cell, N is 1 regardless of how long that TC remains in the grid cell. The average duration (D = Freq/N) is defined as the TC frequency (Freq) normalized by the TC number (N), indicating the average time TCs stay in the grid cell. Similarly, the ACE in a certain grid cell is determined by the effects of both the TC frequency of occurrence and the corresponding intensities. Thus, the average intensity [$I = \sum_{k=1}^{\mathrm{Freq}} V_{\max}^2(k)/\mathrm{Freq}$] can be obtained by the ACE normalized by TC frequency.

3) Statistical test of spectral analysis

To identify the significant periods of AWB variation and jet stream intensity, we analyze the theoretical Markov spectrum (red noise) and its 95% confidence level for the AWB time series. The red noise spectrum S_0 is estimated as shown in Eq. (3):

$$S_0 = \overline{S}\left(\frac{1 - r_1^2}{1 + r_1^2 - 2r_1\cos 2\pi\omega}\right), \tag{3}$$

where ω is the frequency, $\overline{S}$ is the variance of white noise, and r_1 is the lag-1 autocorrelation coefficient of the observed time series. The 95% confidence bound for the red noise spectrum is derived based on the χ^2 distribution

(Ghil et al. 2002). The 95th quantile of the chi-square distribution is widely used to test the significant difference between the spectrum and noise background (i.e., red noise in this study), which assumes that the spectrum is in the context of normal distributions.

4) ROSSBY WAVE ACTIVITY FLUX

To reveal the Rossby wave propagation associated with AWB, the anomalous wave activity flux (WAF) associated with AWB activity is also analyzed following the definition of WAF proposed by Takaya and Nakamura (2001):

$$\mathbf{W} = \frac{p\cos\phi}{2|\mathbf{U}|}\begin{Bmatrix} \frac{U}{a^2\cos^2\varphi}\left[\left(\frac{\partial\psi'}{\partial\lambda}\right)^2 - \psi'\frac{\partial^2\psi'}{\partial\lambda^2}\right] + \frac{V}{a^2\cos\varphi}\left(\frac{\partial\psi'}{\partial\lambda}\frac{\partial\psi'}{\partial\varphi} - \psi'\frac{\partial^2\psi'}{\partial\lambda\partial\varphi}\right) \\ \frac{U}{a^2\cos\varphi}\left(\frac{\partial\psi'}{\partial\lambda}\frac{\partial\psi'}{\partial\varphi} - \psi'\frac{\partial^2\psi'}{\partial\lambda\partial\varphi}\right) + \frac{V}{a^2}\left[\left(\frac{\partial\psi'}{\partial\varphi}\right)^2 - \psi'\frac{\partial^2\psi'}{\partial\varphi^2}\right] \end{Bmatrix}, \quad (4)$$

where $\mathbf{W}$ is the WAF; φ, λ, and a represent the latitude, longitude, and Earth's radius, respectively; p = (pressure/1000 hPa); $\mathbf{U} = (U, V)$ denotes the climatological daily mean of wind fields; and ψ' is the anomalous streamfunction.

To test whether the time-filtering (either the use of a 10-day period or application of a 5-day running mean) is an essential process when studying the subseasonal AWB–TC relationship, we analyzed the unfiltered AWB and its connection with daily ACE. The signals of AWB and ACE are noisier and less organized when the synoptic-scale disturbances are retained, although the connections between AWB and ACE can still be identified as those based on the filtered data. Therefore, the filtering process helps to efficiently recognize the variability of AWB activity and its connection with TCs at the intraseasonal time scale.

3. The subseasonal variability of AWBs over the North Pacific

a. *Basic characteristics of AWBs over the North Pacific*

The spatial distributions of AWBs and their standard deviations during the WNP TC season are displayed in Fig. 1. Like the seasonal AWB distribution over the North Atlantic (Zhang et al. 2017; Li et al. 2018), the intraseasonal AWB frequency maximizes over the equatorward sector of the westerly jet exit (black contours in Fig. 1a). The spatial distribution of the intraseasonal AWB variability is consistent with its climatology (Fig. 1b); both show a southwest–northeast tilted structure over the North Pacific. Unlike the relatively small subseasonal variability of North Atlantic AWBs [Fig. 1 in Li et al. (2018)], the standard deviation of an AWB occurrence is larger than its climatology. This suggests a more prominent variability of AWBs over the North Pacific. To investigate the anomalous large-scale fields associated with the AWB variability and its impact on the subseasonal variability of TC activity over the WNP, we define the active AWB activity domain (10°–30°N, 130°E–150°W; blue boxes in Fig. 1). We select the active AWB domain with a slight westward shift that not only shows the active AWB frequency but also encompasses an active TC region over the North Pacific; however, the large centers of the AWB climatology and standard deviation are located over the central North Pacific.

Figure 2 shows composites of the anomalous large-scale fields relative to the AWB location, whose center (0 on both the x and y axes) is defined by the centroids in the equatorward tongue of the high-PV air region (green contours in Fig. 2). When an AWB occurs, a positive relative vorticity anomaly in the upper troposphere—associated with a high-PV intrusion—is observed near the AWB location (Fig. 2a). Meanwhile, the low-PV air intrudes poleward from low-latitude to high-latitude regions and results in a negative relative vorticity anomaly to the north of the AWB location. The vorticity anomalies at 200 hPa show a northeast–southwest-elongated dipole pattern along with a reversed 2-PVU contour (contours in Fig. 2a). In the lower troposphere, the tripole pattern of vorticity anomalies is clear but is shifted slightly southward compared to the upper-level vorticities (shading in Fig. 2a). Thus, the vorticity perturbations induced by AWBs have a nearly equivalent barotropic structure titling northward with height (Fig. 2a). The vertical motions associated with the AWB affect the moisture transport in the column. In Fig. 2b, the descending (ascending) motion is found in the center (northwest and southwest) of the AWB region. The high-PV intrusion from the high-latitude region induces a drying and cooling effect on the troposphere, contributing to a decreased amount of total precipitable water (contours in Fig. 2b) and a decreased thickness of the free atmosphere (contours in Fig. 2c) between 850 and 200 hPa. Meanwhile, upward motion (shading in Fig. 2b) and positive precipitable water (contours in Fig. 2b) anomalies are observed to the north and southwest of the AWB center favoring convective activities in those regions (blue shading in Fig. 2d). The VWS anomalies also appear in a tripole pattern with a decreased VWS near and to the north of the AWB location and increased VWS anomalies to its north and south (shading in Fig. 2c). These composite results of large-scale fields associated with AWBs are similar to those that have been observed over the North Atlantic (Zhang et al. 2017).

To elucidate the forcing mechanisms associated with the upper-level PV tongue and surface negative relative vorticity anomaly, we composited the relative vorticity (shading) and vertical p velocity (contours) at 200 hPa (shading in Figs. 3a,b) and 850 hPa (shading in Figs. 3c,d) from 5 (Figs. 3a,c) days before and the day when AWBs occur (Figs. 3b,d). The tripole pattern of anomalous relative vorticity at the upper level occurs

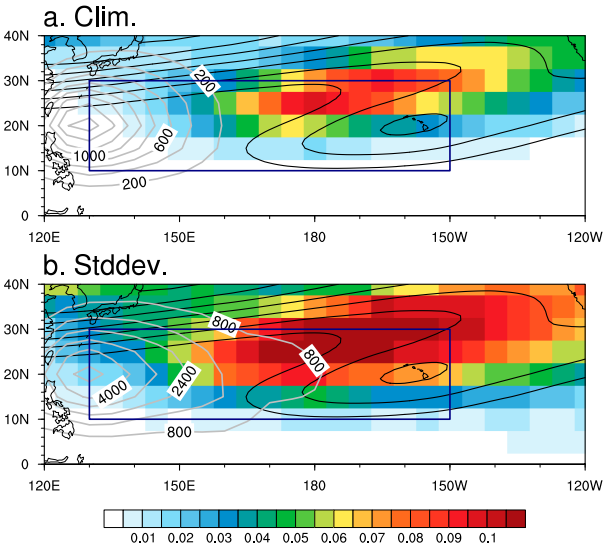

FIG. 1. The (a) climatological mean and (b) standard deviation of the daily 5-day running mean AWB frequency (shading; day^{-1}) and ACE (gray contours; m^2 s^{-2}) derived from JTWC in each 5° × 5° grid cell (shading) during June–November from 1979 to 2020. Climatological zonal winds at 200 hPa (starting at 5 m s^{-1}; interval: 5 m s^{-1}) are superimposed as black contours. The blue frame delineates the active AWB domain (10°–30°N, 130°E–150°W) over the North Pacific.

5 days before AWBs occur (Fig. 3a), during which almost no significant signal of anomalous relative vorticity exists at the lower level (Fig. 3c). From 5 days before until AWBs occur, the anomalous relative vorticity (shading in Figs. 3a,b) and downward motion (contours in Figs. 3a,b) at the upper level are both larger than those at the low level. Besides, the vertical p-velocity at 200 hPa (contours in Figs. 3a,b) is larger than that at 850 hPa (contours in Figs. 3c,d), which results in a negative value of $\partial\omega/\partial p$ from 5 days before until AWBs occur. This negative value of $\partial\omega/\partial p$ indicates that the downward motion is divergent and contributes to the lower-level anticyclonic anomalies. All these results suggest that the upper-level forcing of AWB impacts the lower-level conditions and contributes to enhancement of the anticyclone in the lower troposphere. Similar results were also documented by Zhang et al. (2017) and Takemura and Mukougawa (2020a,b).

b. *Subseasonal variability of AWBs*

To examine whether the AWB frequency of occurrence shows a significant intraseasonal signal within the TC seasons, we performed a spectral analysis of the intraseasonal area-averaged AWB frequency over the active AWB domain (10°–30°N, 130°E–150°W). For convenience, we refer to the aforementioned time series as the AWB index. Using the climatological AWB index (green curve in Fig. 4a) and its variation in an arbitrary year (say, the year 2000; black curve in Fig. 4a) as an example, we find that the AWB occurrence is climatologically more vigorous during the summer (June–September) than the autumn (October–November; green curve in Fig. 4a), as documented by Abatzoglou and Magnusdottir (2006) and Bowley et al. (2019). Within the year-2000 TC season, the AWB index shows strong subseasonal variations (shading in Fig. 4a). To identify the dominant period of intraseasonal AWB variability, a power spectrum analysis of the daily AWB index is conducted for each year, and the average spectrum over the 42 TC seasons of 1979–2020 is illustrated. The results show that the AWB occurrence varies significantly with a period of 7–40 days (Fig. 4b).

Next, we present the spatiotemporal evolution of the large-scale circulations associated with AWBs and the Rossby wave dynamics (Figs. 5 and 6). Day 0 is defined as the time at which the AWB index exceeds one standard deviation and reaches its maximal value (the daily AWB index at time t is larger than that at $t - 1$ and $t + 1$). There are 405 days identified as day 0 during the TC seasons (June–November) for 1979–2020. The lead and lag daily anomalies are composited from day −12 to day 9. When the AWB is active (day 0), the local circulation anomalies are characterized by a low pressure anomaly over the tropical WNP and a high pressure anomaly near the subtropical date line region (Fig. 5a), similar to the result shown in Fig. 2a. A Hovmöller diagram of the 200-hPa meridional wind and streamfunction anomalies averaged between 30° and 50°N shows a wave train structure, which is most evident (Fig. 5a) from day −15 to day 3 (Fig. 5b). A quasi-stationary Rossby wave pattern (a couplet of cyclonic and anticyclonic anomalies) is found over 30°–80°E from day −12 to day −6. From day −9, an eastward-propagating WAF (black vectors) appears around this wave area, suggesting the emanation of Rossby wave energy toward the downstream region over northern Asia and the western-central North Pacific. Thus, the wave patterns over 100°E–160°W initiate from around day −6 to day −3 and strengthen with time. The high pressure anomaly around 180° reaches its maximum amplitude around day 0, when the AWB occurs. The wave train associated with AWB over the North Pacific is similar to the composite results in Fig. 4 of Takemura and Mukougawa (2020a) and those over the North Atlantic in Fig. 2 of Li et al. (2018). To investigate whether the significant ridging signal early on day −9 over the North Pacific (Fig. 5b) is a local precursor to AWB or results from a cyclical AWB, we analyzed the evolution of AWB frequency anomalies from day −12 to day 6 (yellow bars in Fig. 5c) and found that the evolution of AWB frequency over the North Pacific becomes significant only between day −4 and day 4, without any significant signals during the earlier stage (from day −12 to day −5). This result suggests that the positive geopotential anomalies early on day −9 over the North Pacific (Fig. 5b) are a local precursor to AWB.

The occurrence of AWB is related to a significant weakening and northeastward shift of the climatological jet stream over its existing region (Fig. 6e). Compared to the climatology (red contours), the westerly jet stream (blue contours of 30 m s^{-1}) begins to elongate northeastward (Figs. 6b,c) and the maximum center of the westerly jet (blue contours of 35 m s^{-1}) weakens from day −9 to day −6, accompanied by a negative zonal wind anomaly in the equatorward flank of the jet stream (shading in Figs. 6b,c). From day −3 to day 0 (Figs. 6d,e), the continual northeastward shift of the westerly jet induces a larger negative zonal wind anomaly on the equatorward side of the exit region (shading in Figs. 6d,e), which is close to the active AWB region (blue frames in Fig. 6). The strength and location of the westerly jet associated with AWB occurrence change consistently along with the enhanced equatorward Rossby WAF (Figs. 6a–d). When

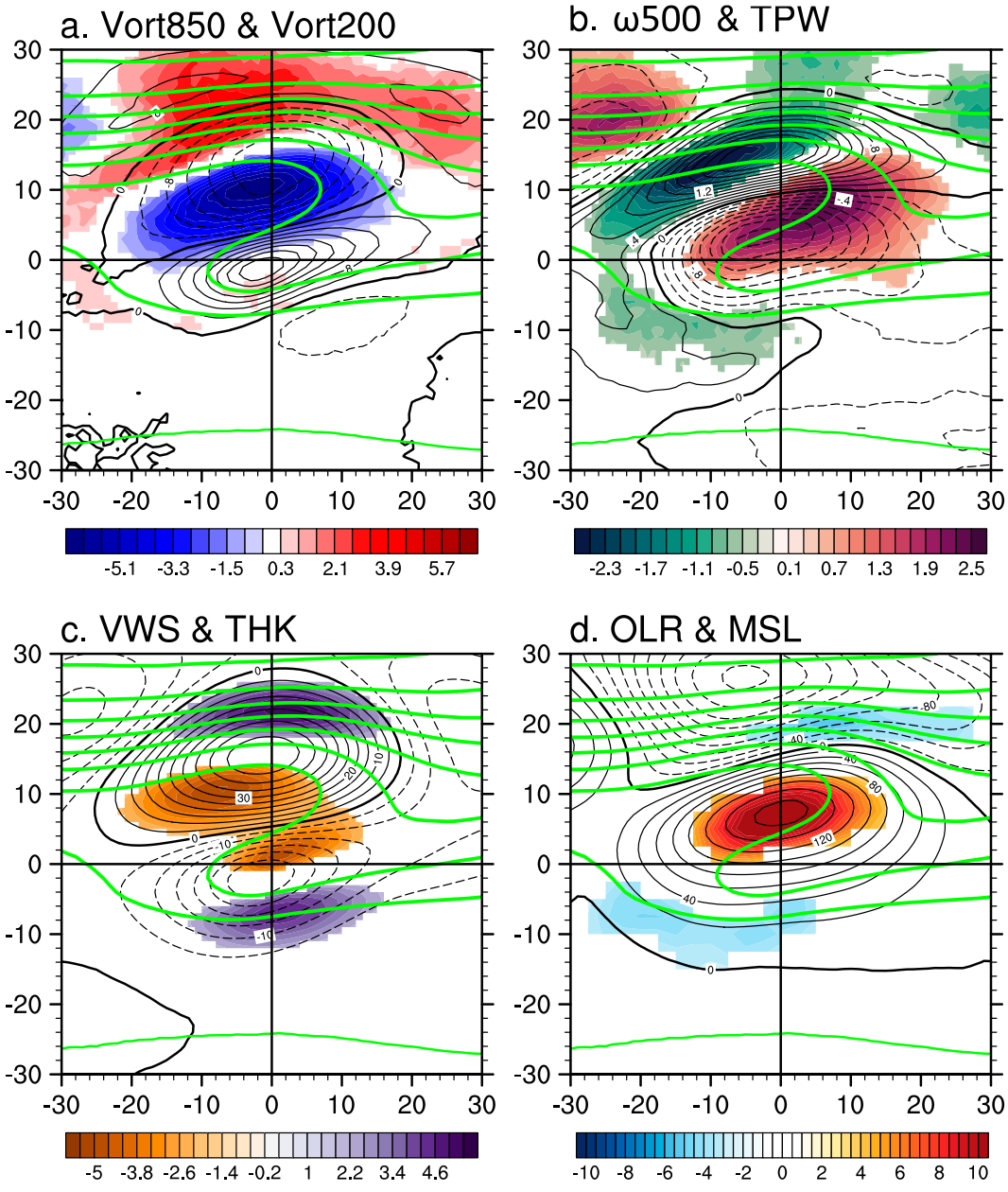

FIG. 2. Composites of the daily anomalous (a) relative vorticity at 850 hPa (Vort850; shading; 10^{-6} m s^{-2}; only regions with significant changes at the 95% confidence level are shown) and 200 hPa (Vort200; black contours from -40 to 40 with an interval of 4×10^{-6} m s^{-2}), (b) vertical velocity at 500 hPa (ω500; shading; 10^{-2} Pa s^{-1}; only regions with significant changes at the 95% confidence level are shown) and free-tropospheric total precipitable water (TPW; black contours from -2 to 2 with an interval of 0.2 mm), (c) VWS (shading; m s^{-1}; only regions with significant changes at the 95% confidence level are shown) and thickness (THK; black contour; contours from -50 to 50 with an interval of 5 m) between 200 and 850 hPa, and (d) OLR (shading; W m^{-2}; only regions with significant changes at the 95% confidence level are shown) and mean sea level pressure (MSL; black contours from -160 to 160 with an interval of 20 Pa) centered at AWBs over the active AWB domain (black box in Fig. 1). Positive and negative values are in solid and dashed lines, respectively. Green contours in (a)–(d) are PVU contours starting from 0 PVU with an interval of 1 PVU (1 PVU = 10^{-6} K kg^{-1} m^2 s^{-1}). The total number of AWBs is 16 949.

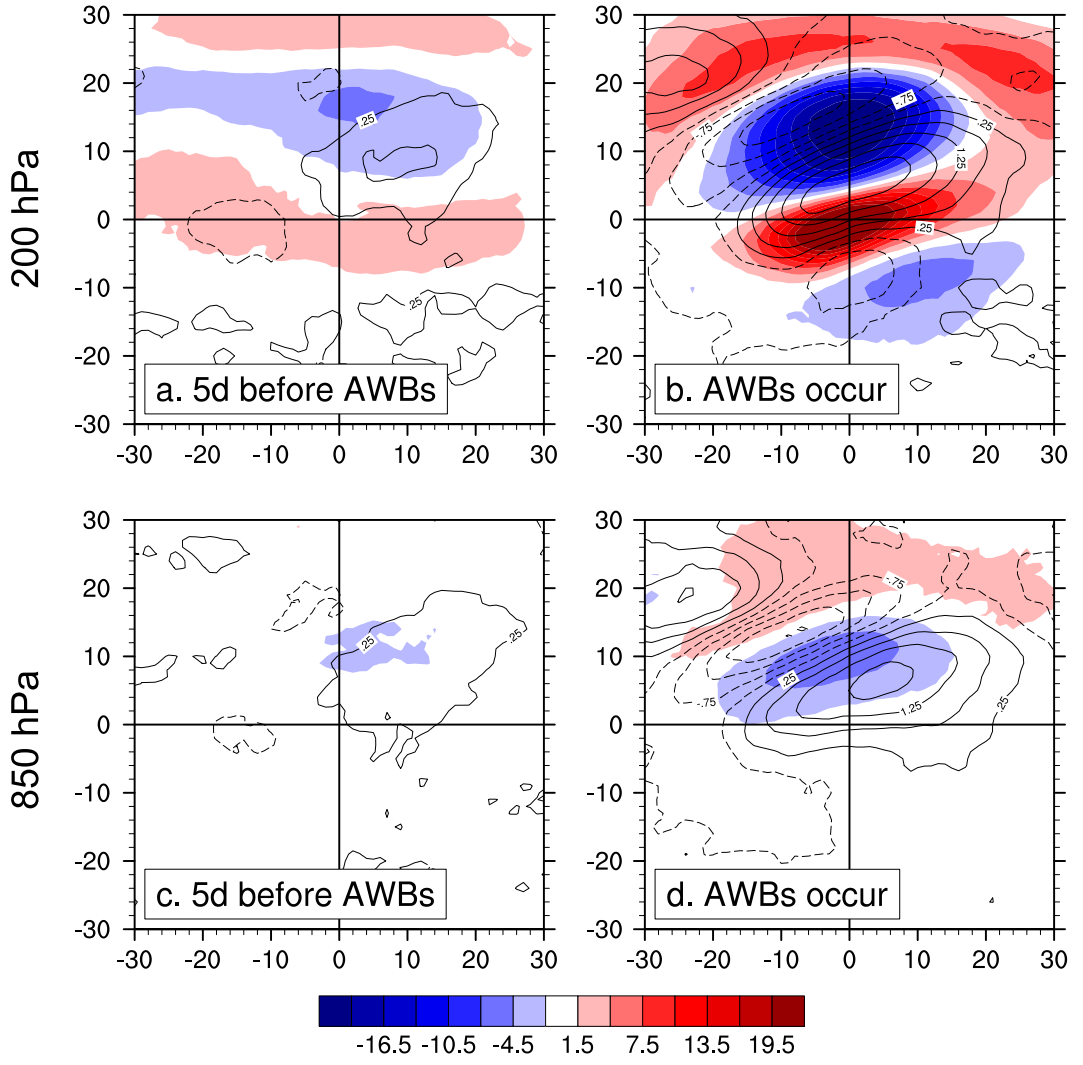

FIG. 3. Composites of the daily anomalous relative vorticity (shading; 10^{-6} m s^{-2}; only regions with significant changes at the 95% confidence level are shown) and vertical p velocity (contours from -2.25×10^{-2} to 2.25×10^{-2} Pa s^{-1} with an interval of 0.5 Pa s^{-1}) at (a),(b) 200 and (c),(d) 850 hPa for (left) 5 days before and (right) the day AWBs occur.

the AWB frequency is reduced from day 3 to day 9, the Rossby wave train gradually dissipates (Fig. 5b). Meanwhile, the jet intensity is strengthened, and the equatorward WAF fades away (Figs. 6f–h). These plots confirm the intraseasonal AWB variations driven by changes in jet stream activity (Fig. 4c). The linkage between AWB and jet stream was also documented in previous studies (Woollings et al. 2011; Zhang and Wang 2018), in which the poleward movement of the jet stream associated with the amplified and persistent ridge at upper level was highlighted.

In addition to the anomalous large-scale fields associated with the AWB in the midlatitude region, significant tropical signals are also found. Around 12 days prior to the AWB occurrence, a convective anomaly appears in the equatorial south Indian Ocean (Fig. 6a). From days −12 to 0, this convection moves northward and northeastward toward the north Indian Ocean and the South China Sea (SCS, Figs. 6b–d), lying to the south of the wave train anomalies over the North Pacific. To show the relationship between tropical OLR and AWB activity, we plotted the anomalous OLR over the tropics (5°–25°N, 50°–130°E) and nondivergent wind (represented by the streamfunction) at 200 hPa over the active AWB domain (10°–30°N, 130°E–150°W) associated with AWB activities (not shown). The result shows that the tropical convection (negative OLR anomaly) emerges on day −14 and enhances thereafter, reaching its maximum on day −1. In the meantime, the negative streamfunction at 200 hPa associated with AWB activity becomes negative on day −7 and decreases rapidly to its minimum on day 0. The phase transition for the streamfunction is faster than that of OLR, suggesting that the former has a shorter period. Even so, the temporal correlation coefficient between the OLR and streamfunction is 0.97, statistically significant at the greater than 99% confidence level. These results indicate that the variance of AWB is likely related to the shift in evolution

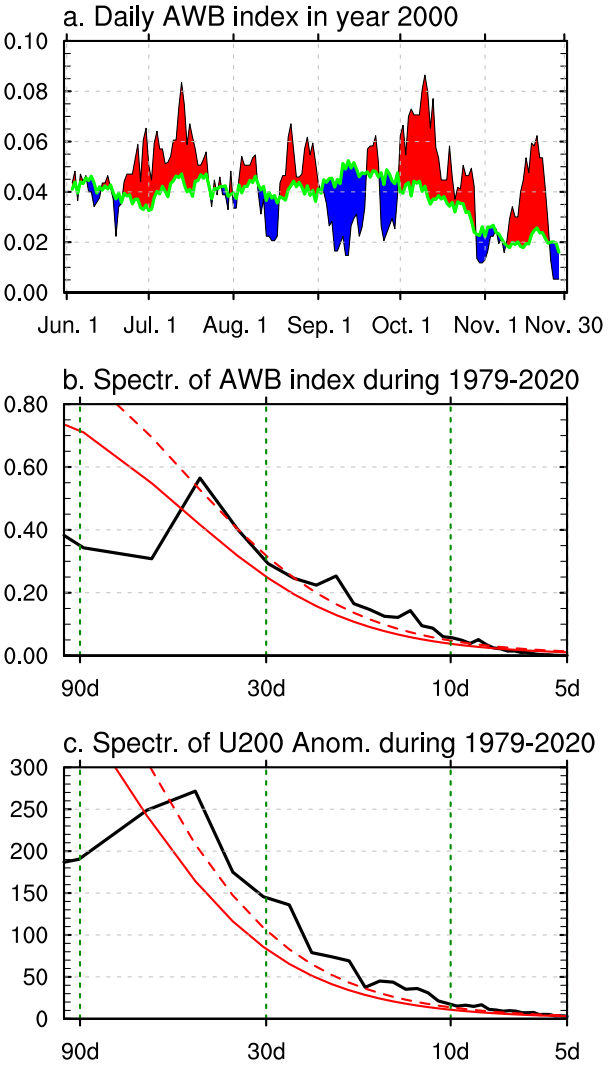

FIG. 4. (a) Time series of the intraseasonal anomalous AWB frequency (day^{-1}; red and blue shading) averaged over the active AWB domain (10°–30°N, 130°E–150°W) in the year 2000 relative to the climatological mean state (green contour). (b),(c) Power spectrum of the (b) daily AWB index (10^{-2} day^{-2}) and (c) zonal wind anomaly (m^2 s^{-2}) averaged over the active AWB domain (black box in Fig. 1) during the TC seasons of 1979–2020. The red solid and dashed lines represent the red noise spectrum and the 95% confidence level based on the χ^2 distribution, respectively.

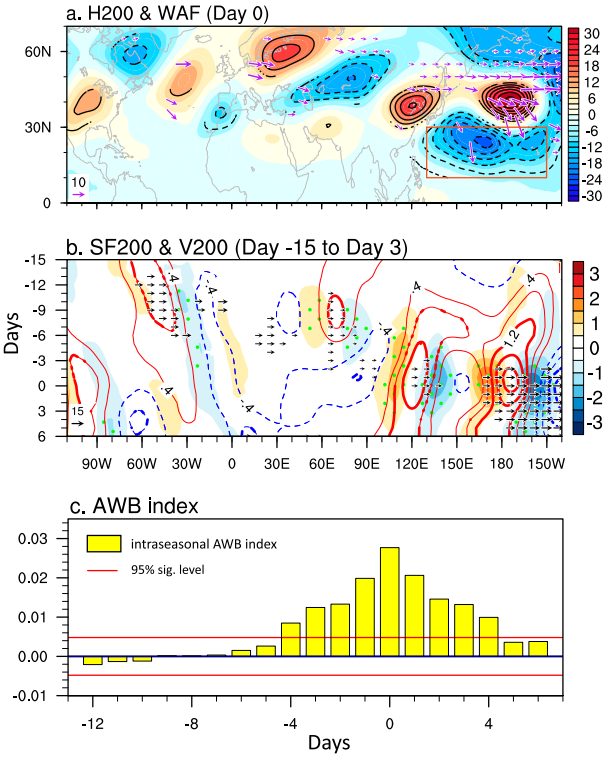

FIG. 5. (a) Composites of intraseasonal (5-day running mean) geopotential height anomalies (shading; regions with significant changes at the 95% confidence level are shown as solid and dashed contours for positive and negative values, respectively, with an interval of 4 gpm) and intraseasonal WAF (purple vectors; m^2 s^{-2}; only regions with significant changes at the 95% confidence level are shown) at 200 hPa on day 0. The red box indicates the active AWB domain (10°–30°N, 130°E–150°W). (b) Hovmöller diagram of intraseasonal meridional wind anomalies (shading; m s^{-1}) and streamfunction anomalies (contours; 10^{-6} m^2 s^{-1}; regions with significant changes at the 95% confidence level are shown as thick contours), and the zonal component of the WAF anomaly (black vectors; m^2 s^{-2}; only regions with significant changes at the 95% confidence level are shown) at 200 hPa averaged between 30° and 50°N from day −15 to day 5. Green dots indicate that the changes in the 200-hPa streamfunction anomalies are significant at the 95% confidence level. (c) Composite of the intraseasonal AWB index (yellow bars) from day −12 to day 6. Red lines indicate that the changes in intraseasonal AWB index are significant at the 95% confidence level.

of tropical convection. The effects of tropical convection on AWB occurrence have been found during boreal winter (MacRitchie and Roundy 2016) and summer (Li et al. 2018).

In summary, the results of Fig. 6 show that AWB activity is associated with perturbations in both the jet stream and tropical convection. However, we believe that the former plays a more significant role in modulating AWB activity because the occurrence of AWB is commonly attributed to phenomena associated with the interaction between the Rossby wave and the jet stream (Rivière et al. 2010; Franzke et al. 2011). Although the composited results display tropical convection anomalies alongside AWB occurrence, their actual co-occurrence rate is approximately 70.6% (which will be discussed in detail in section 4c). This suggests that tropical convection perturbations may influence AWB occurrence but are not considered essential factors. Wang et al. (2022) indicated that the eastward-propagating wave train related to AWB occasionally occurs in association with this tropical intraseasonal convection. This tropical convection may be associated with the maintenance of AWB and an enhanced Pacific–Japan pattern (Takemura and Mukougawa 2020a,b), which suggests a more complex relationship between AWBs and TC activity over the WNP, because the tropical intraseasonal convection may also directly modulate WNP TCs. Whether the intraseasonal convection anomaly over the north Indian Ocean and SCS is essential to

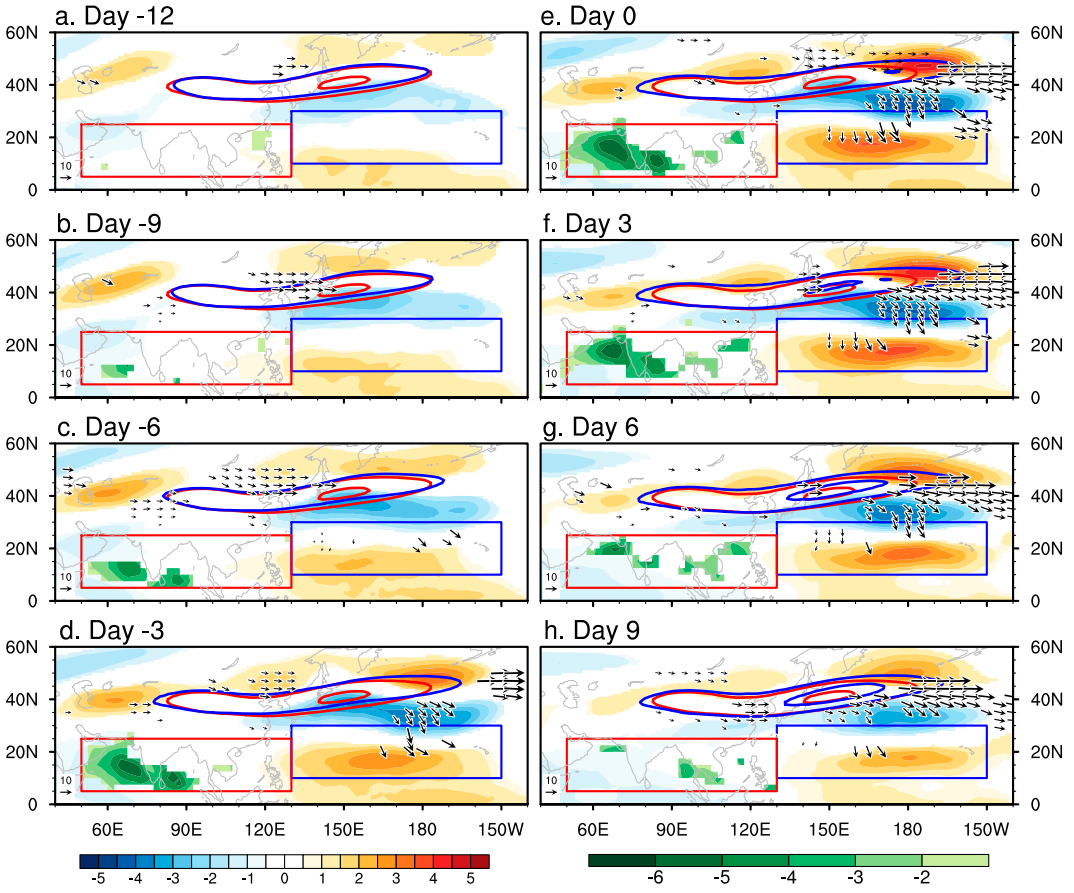

FIG. 6. Composites of the intraseasonal zonal wind (blue contours; starting from 30 m s^{-1} and with an interval of 5 m s^{-1}) and their anomalies (red and blue shading; m s^{-1}; only regions with significant changes at the 95% confidence level are shown), and anomalous WAF (black vectors; m^2 s^{-2}; only regions with significant changes at the 95% confidence level are shown) at 200 hPa, and negative intraseasonal OLR (green shading; only regions with significant changes at the 95% confidence level are shown), on days (a) −12, (b) −9, (c) −6, (d) −3, (e) 0, (f) 3, (g) 6, and (h) 9. The climatological mean of the zonal wind (starting from 30 m s^{-1} and with an interval of 5 m s^{-1}) at 200 hPa, representing the westerly jet, is shown as a red contour. The blue frame marks the active AWB domain (10°–30°N, 130°E–150°W). The red frame indicates the active tropical convection domain (5°–25°N, 50°–130°E).

the AWB-induced TC activity changes will be discussed in the next section.

4. AWB modulation of WNP TC activity at intraseasonal time scales

a. AWB intraseasonal modulation of TC activity

To focus on the AWB–TC relationship at the intraseasonal time scale, the AWB index was first totaled over each 10-day period to ignore its synoptic variability, as with the TC-related indices. Then, an index called AWBisv, which presents the intraseasonal AWB anomaly, is defined as the AWB anomaly normalized by climatological running-mean standard deviations derived from the whole period from 1 June to 27 November during 1979–2020. The 10-day total AWB index and AWBisv index are compared in Fig. 7a, in which the positive and negative AWB phases are defined as being when AWBisv is larger than 1 and smaller than −1, respectively. The neutral AWB phase is defined as being when AWBisv is larger than −1 and smaller than 1. There are 129 (119) 10-day periods defined as positive (negative) AWB phases, accounting for 17.06% (15.74%) of the total 756 AWBisv cases.

Next, we compare the effects of AWBs on TC activities on intraseasonal time scales by compositing the ACE for different AWB phases (Fig. 8). The two best track datasets (JTWC and RSMC) consistently show that negative ACE anomalies are observed over most of the WNP open ocean, while there are positive ACE anomalies over the SCS and Philippine Sea, during the AWB positive phase (Figs. 8a,e), indicating robust modulations of AWB on the subseasonal TC activities over the WNP. An opposite pattern, however, is seen in the AWB negative phase (absence of AWB frequency; Figs. 8b,f). The results suggest that AWBs exert a negative impact on TC activities over the open ocean of the WNP but slightly benefit TC activities in the SCS (Figs. 8c,g). To quantify the effects of AWB on TCs, we computed the percentage changes of ACE relative to the climatological

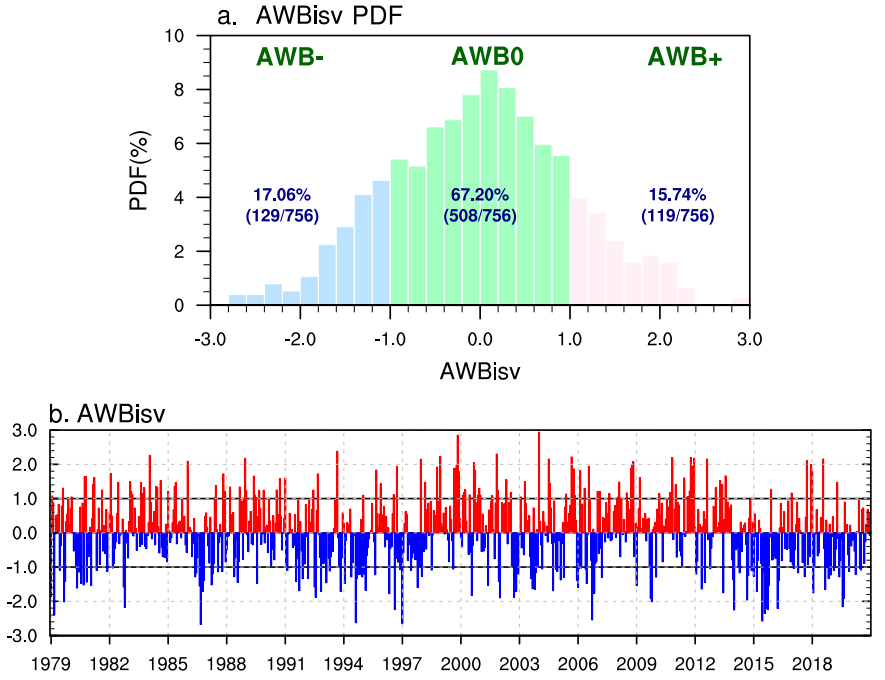

FIG. 7. (a) The probability distribution of AWBisv index (%). The percentages and numbers of different categories relative to total cases (values in parentheses) are also shown. Red and blue bars indicate the positive and negative AWB phases. (b) Time series of AWBisv from 1 Jun to 27 Nov during 1979–2020.

mean modulated by AWB (Figs. 8d,h). The AWB-induced change in ACE over the WNP open ocean derived from JTWC (RSMC) is $-414.7\ m^2\ s^{-2}$ ($-376.5\ m^2\ s^{-2}$), accounting for −102.9% (−138.7%) of the change relative to the climatological mean. Compared to the WNP open ocean, the change in ACE over the SCS as modulated by AWB activities is smaller, being 381.7 and 297.7 $m^2\ s^{-2}$ derived from JTWC and RSMC, respectively, and contributing to 57.2% and 61.0% of the changes relative to the climatological mean.

To further understand the relative contributions of the TC activities to the ACE changes modulated by AWB, we decomposed ACE into the TC number, average duration, and average intensity relative to the total change in ACE [Eq. (1)]. Each TC metric in the positive AWB phases (X_p) can be represented by the TC metrics in the negative AWB phases (X_n) and the changes in X relative to the negative AWB phases (ΔX). That is, $X_p = X_n + \Delta X$, where X represents ACE and each component in Eq. (2), such as N, D, and I. Thus, the change in ACE between the positive and negative AWB phases and the associated contribution terms can be written as follows:

$$\begin{aligned}\Delta\mathrm{ACE} &= \mathrm{ACE}_p - \mathrm{ACE}_n \\ &= [(N_n + \Delta N)(D_n + \Delta D)(I_n + \Delta I)] - N_n D_n I_n \\ &= \Delta N D_n I_n + N_n \Delta D I_n + N_n D_n \Delta I + \Delta N \Delta D I_n \\ &\quad + \Delta N D_n \Delta I + N_n \Delta D \Delta I + \Delta N \Delta D \Delta I. \end{aligned} \tag{5}$$

The first, second, and third terms on the rhs of Eq. (5) represent the changes in ACE due to the effects of the changes in TC count, duration, and intensity between the positive and negative phases of AWB. The fourth to seventh terms on the rhs of Eq. (5) indicate the nonlinear effects, including the combined effects of changes in TC count, average duration, and average intensity.

The change in ACE (Fig. 9a) is highly consistent with the differences in ACE between the positive and negative AWB phases (Figs. 8c,g). The reduced ACE over the open ocean of the WNP is mainly attributable to the contributions of TC count (Fig. 9b), average duration (Fig. 9c), and average intensity (Fig. 9d). These three terms also show small positive contributions to the increased ACE over the SCS (Figs. 9b–d). By calculating the area-averaged values over key domains in the open ocean (pink bars in Fig. 9f) and SCS (blue bars in Fig. 9f), we found that the contributions of TC count, intensity, and duration are comparable. The nonlinear process plays a positive role in the ACE changes modulated by AWB (Fig. 9e).

b. *Physical mechanisms for AWB-induced TC activity change*

To understand the physical processes responsible for the changes in ACE modulated by the AWB phases, the differences in the large-scale variables between the positive and negative phases of AWB were composited. Compared with the negative AWB phase (reduced frequency of AWB occurrence), a significant upper-tropospheric low pressure anomaly is observed over

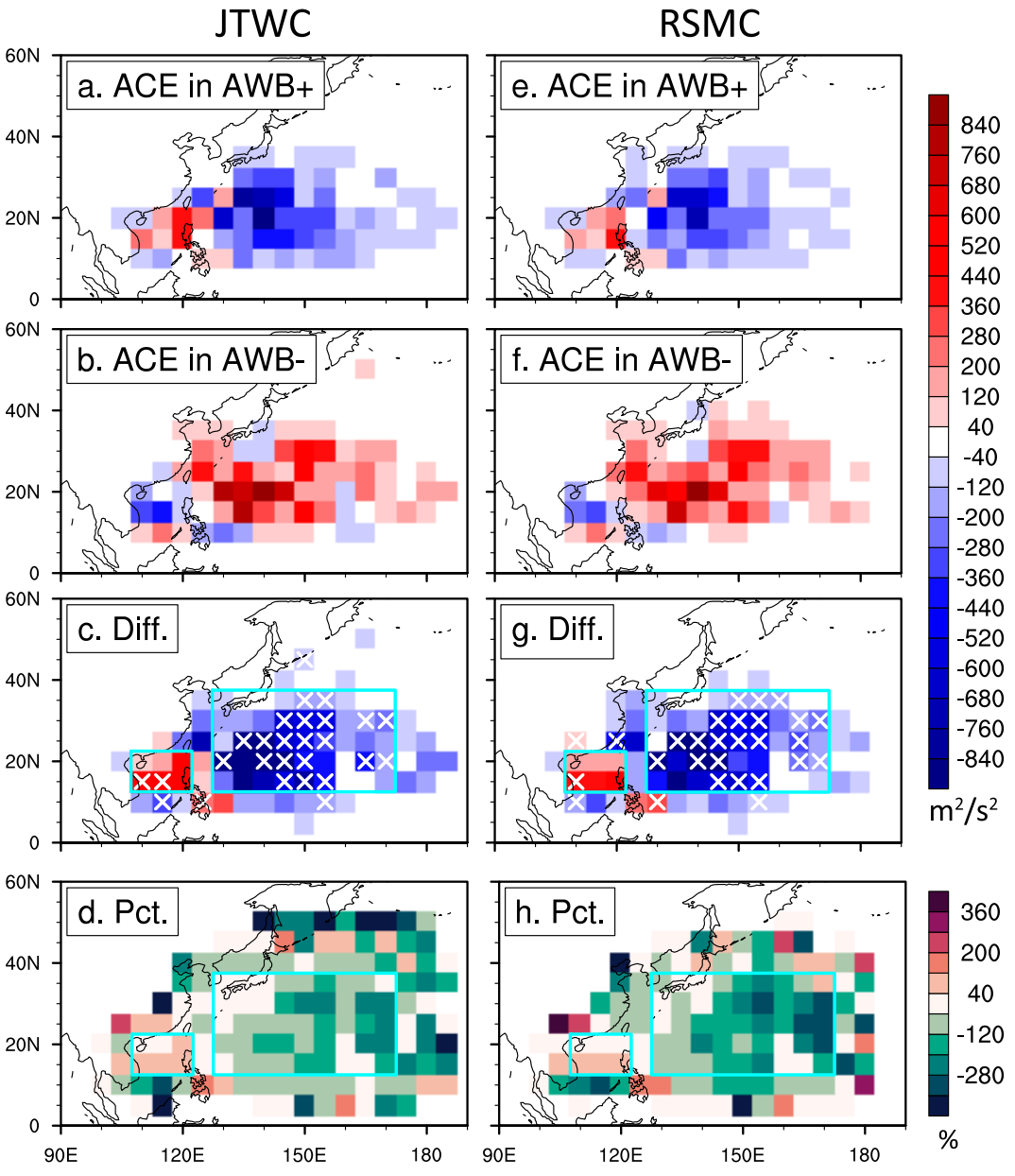

FIG. 8. Accumulated cyclonic energy (ACE) anomalies in the (a) positive and (b) negative AWB phases and (c) their difference ($m^2 s^{-2}$). (d) The percentage change relative to the climatological mean (%) derived from JTWC. (e)–(h) As in (a)–(d), but for the results from the RSMC dataset. The white crosses in (c) and (f) denote regions with significant ACE differences at the 95% confidence level. The cyan frames in (c),(d) and (g),(h) mark the key regions of the WNP open ocean (12.5°–37.5°N, 127.5°–172.5°E) and SCS (12.5°–22.5°N, 107.5°–122.5°E) in which ACE was influenced by AWB.

the WNP open ocean (red frame in Fig. 10a) during the positive phase of the AWB, when a high-PV intrusion associated with enhanced AWB activity occurs. This cyclonic anomaly may be closely related to the tropical upper-tropospheric trough feature discussed in Wang et al. (2020). High pressure anomalies are observed from the subtropical WNP to eastern China, which results from the poleward low-PV intrusion from the tropics (Fig. 10a). In the meantime, a positive lower-tropospheric high pressure anomaly is centered over the subtropical north central Pacific (35°N, 180°) and nearly covers the entire subtropical WNP in the lower troposphere (Fig. 10b). The poleward tilting of the geopotential height anomaly over the tropical–subtropical region can clearly be seen in the vertical profile of the geopotential height anomaly (Fig. 11e). The westward tilt of the geopotential height around 90°–127.5°E indicates a baroclinic vertical structure (Fig. 11a), accompanied by upward motion (Fig. 11b) and increased humidity (Fig. 11c), which is conducive to the development of convection and TC activity. In contrast, the

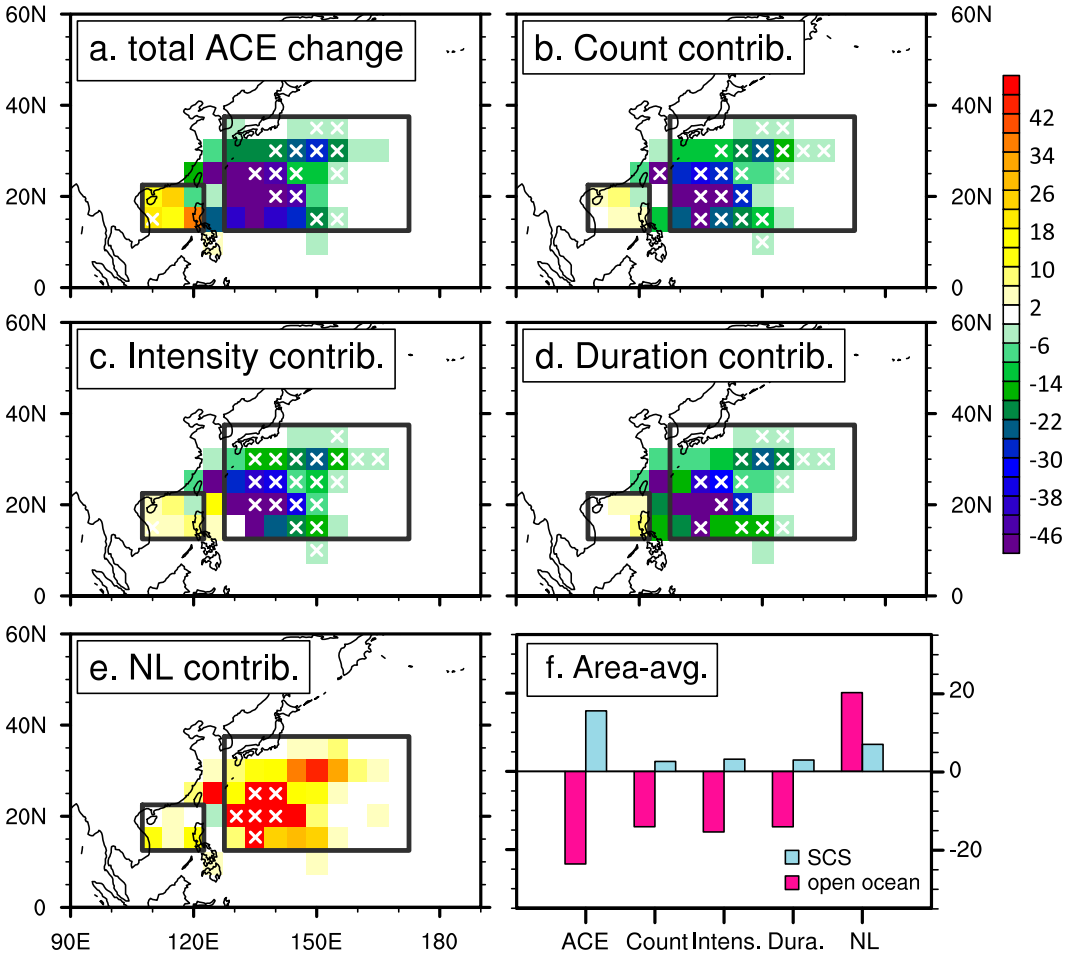

FIG. 9. (a) Differences in the total change in ACE, and the contributions of (b) TC count, (c) average intensity, (d) average duration, and (e) nonlinear terms between the positive and negative AWB phases ($m^2\ s^{-2}$). Statistically significant changes at the 95% confidence level are marked with white crosses. Red boxes indicate the WNP open ocean (12.5°–37.5°N, 127.5°–172.5°E) and SCS (12.5°–22.5°N, 107.5°–122.5°E) region. (f) The bars from left to right are the area-averaged values over (a)–(e) the WNP open ocean (pink bars) and SCS (light-blue bars), respectively.

equivalent barotropic atmosphere in the ridge (around 127.5°–150°E) characterizes a relatively stable atmospheric stratification, downward motion, and decreased humidity, which suppresses TC activities. Consistent with the local composite of VWS, as shown in Fig. 2c, a meridional tripole structure of VWS anomalies can also be observed over the WNP. This meridional tripole pattern is characterized by positive westerly wind shear anomalies in the southeastern quadrant of the WNP and north of 45°N, and a horseshoe-shaped area of negative wind shear (Fig. 10c). Positive relative vorticity advection from extratropical region associated with AWB activity induces a convergence circulation (Figs. 10a and 11a,e) and results in subsidence (Figs. 10d and 11b,f) over the WNP open ocean. Accompanying the descending motion, other statistically significant anomalies include a negative relative vorticity anomaly (Fig. 10e), decreased total precipitable water (Fig. 10f), and an anomalous drying effect from the middle to the lower levels of the troposphere (Figs. 11d,h). The intrusion of air from the higher latitudes also induces a negative temperature anomaly throughout the troposphere (Figs. 11c,g) and decreases the thickness of the 850–200-hPa layer (Fig. 10g) over the WNP open ocean. The maximum center of the negative temperature anomaly is observed over the northeast of WNP open ocean in the upper troposphere (Figs. 11c,g), which may also intensify the meridional temperature gradient and then the VWS (Fig. 10c). These large-scale fields together produce an unfavorable environment for TC activity. Moreover, an anomalous northerly wind over the WNP constrains the TC from moving northwestward from the tropics (Fig. 10h).

The enhanced TC activity over the SCS is also closely linked with large-scale environmental changes associated with AWB. During a positive AWB phase, anomalous ascending motion (Figs. 10d and 12a,c), increased total precipitable water (Fig. 10f), and specific humidity (Figs. 12b,d) tend to appear over the SCS. Similar results were documented by Takemura and Mukougawa (2021). The diagnosis of Takemura and Mukougawa (2020a,b) suggested that the ascending motion associated with AWB occurrence can mainly be attributed to the differential anomalous vorticity advected by the climatological wind between the upper and

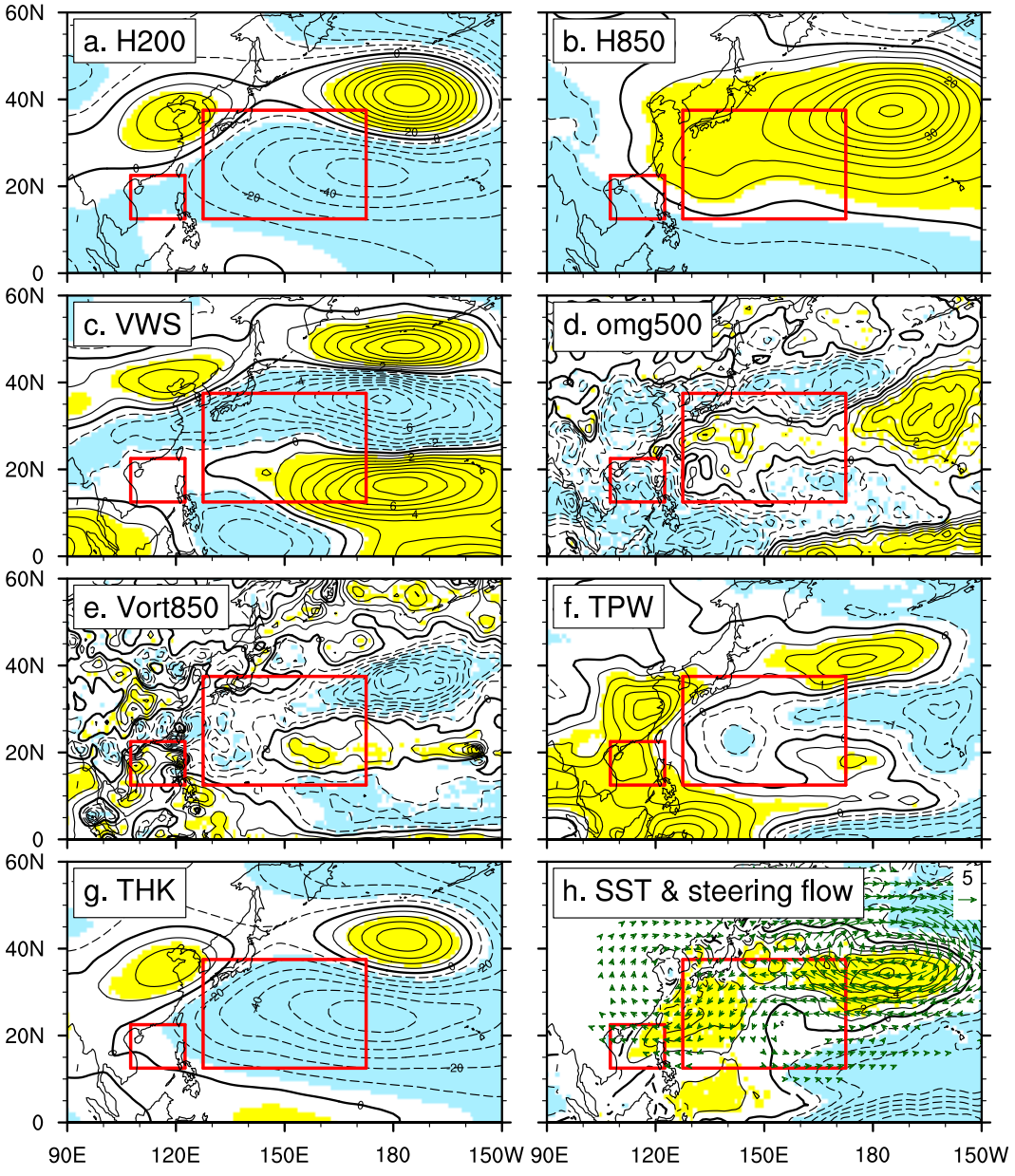

FIG. 10. Changes in the anomalous geopotential height at (a) 200 hPa (interval: 10 gpm) and (b) 850 hPa (interval: 5 gpm), (c) VWS between 850 and 200 hPa (interval: 1 m s^{-1}), (d) 500-hPa vertical velocity (interval: 0.5 × 10^{-2} Pa s^{-1}), (e) relative vorticity at 850 hPa (interval: 10^{-6} s^{-2}), (f) total precipitable water between 850 and 200 hPa (interval: 0.5 mm), (g) thickness between 850 and 200 hPa (interval: 10 m), and (h) SST (interval: 0.1 K) and steering flow (green vectors; m s^{-1}) during the positive AWB phase relative to the negative AWB phase (i.e., positive minus negative). Yellow and light-blue shading indicate that positive and negative anomalies, respectively, are significant at the 95% confidence level. The red frames indicate the WNP open ocean (12.5°–37.5°N, 127.5°–172.5°E) and SCS (12.5°–22.5°N, 107.5°–122.5°E) regions.

lower troposphere. The midtropospheric temperature advection shows a relatively small contribution.

In summary, the results regarding the AWB's modulation of the subseasonal variability of TCs are not uniform over the WNP and depend on the local anomalies induced by AWB. TC activities—including the ACE, TC count, average intensity, and average duration—become inactive over the WNP open ocean but more active over the SCS and Philippines when enhanced AWB frequency occurs.

c. *Relative impacts of tropical convection and AWB on TC activity*

Previous analyses of the effects of AWB on TC activity have been based on the AWB phases; however, this approach cannot

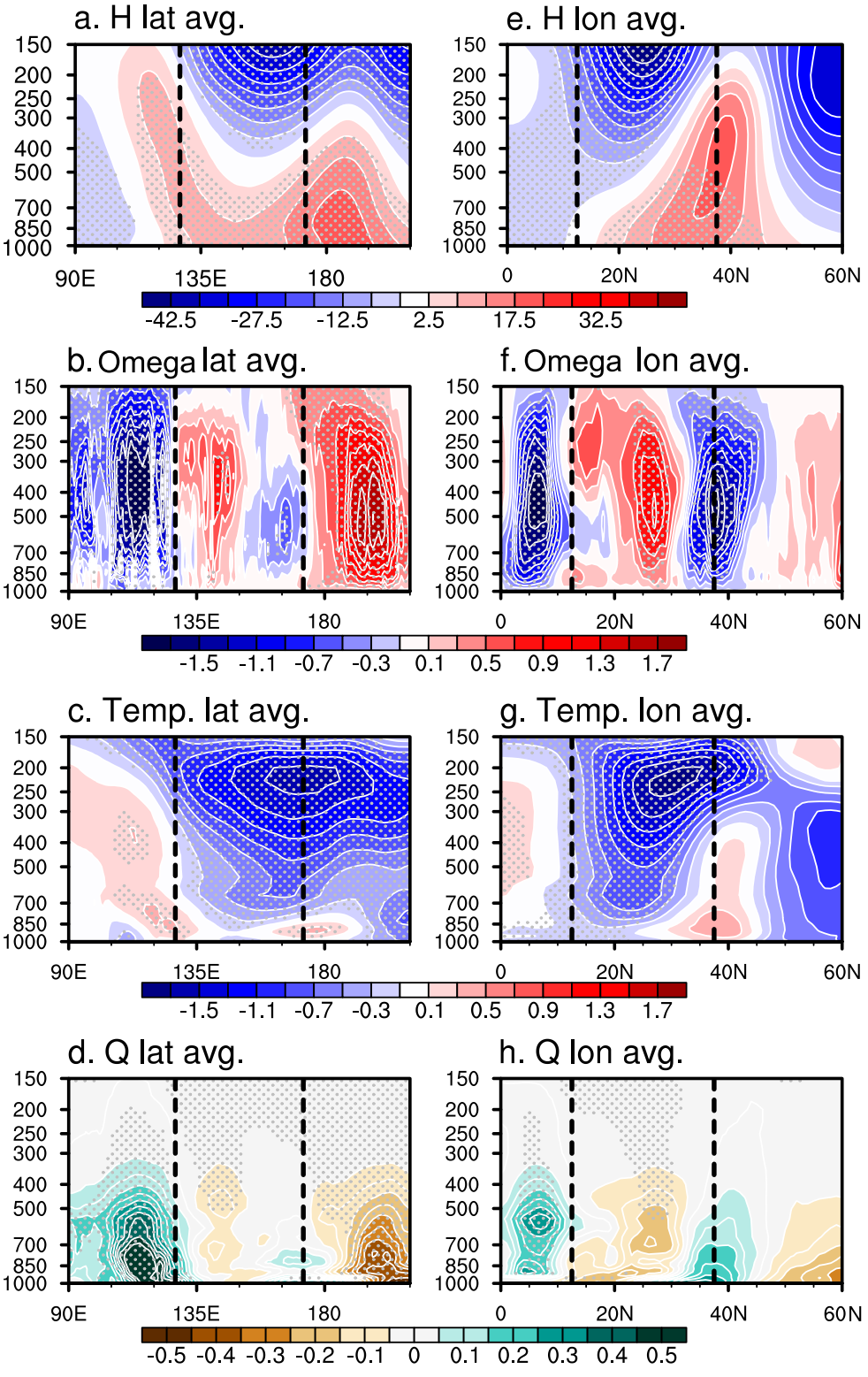

FIG. 11. Vertical–longitude profiles of the zonally averaged (12.5°–37.5°N) anomalous (a) geopotential height (gpm), (b) vertical velocity (Pa s^{-1}), (c) temperature (K), and (d) specific humidity (g kg^{-1}). The vertical dashed lines in (a)–(d) indicate the longitudes of 127.5° and 172.5°E. (e)–(h) As in (a)–(d), but for the vertical–latitude profiles along the longitudes of 127.5°–172.5°E. The vertical dashed lines in (e)–(h) indicate the latitudes of 12.5° and 37.5°N. Regions marked with gray stippling indicate significant changes at the 95% confidence level.

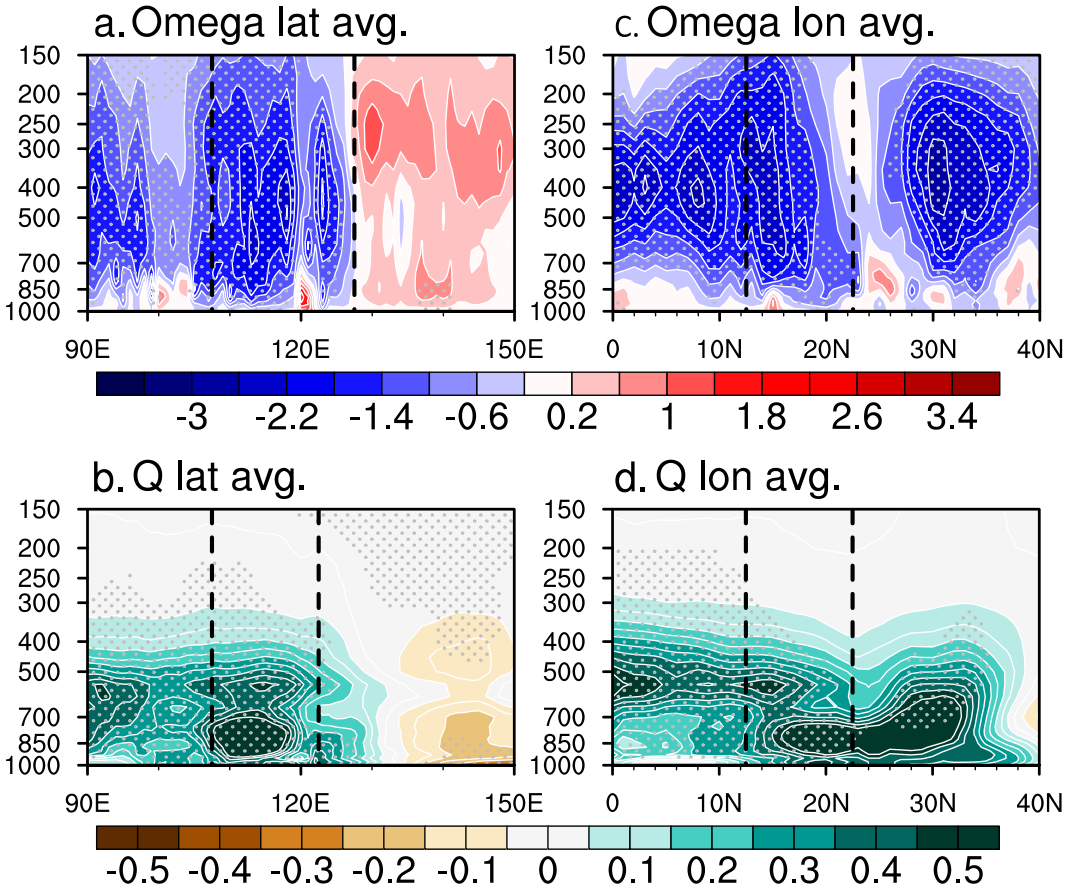

FIG. 12. Vertical–longitude profiles of the zonally averaged (12.5°–22.5°N) anomalous (a) vertical velocity (Pa s^{-1}) and (b) specific humidity (g kg^{-1}). The vertical dashed lines in (a) and (b) indicate the longitudes of 107.5° and 122.5°E. (c),(d) As in (a) and (b), but for the vertical–latitude profiles along the longitudes of 107.5°–122.5°E. The vertical dashed lines in (c) and (d) indicate the latitudes of 12.5° and 22.5°N. Regions marked with gray stippling indicate significant changes at the 95% confidence level.

rule out the tropical effects that work in combination with the extratropical AWBs. For example, tropical convection anomalies are observed over the north Indian Ocean and SCS concurrently with AWBs (Fig. 6e). One question raised is whether the influence of AWBs on TC activities requires the aid of tropical convection signals (red frames in Fig. 6). In other words, could AWB modulate TC activity through its related large-scale anomalies (Figs. 8–12) without the effects of tropical convection? To answer this, we separated all AWBisv samples (756 samples = 18 × 42 years) into cases that involved active tropical convection (active convection cases, 222 samples) and those that did not (inactive convection cases, 534 samples). Note that active/inactive tropical convection was defined as occurring when the normalized 10-day-averaged 10–90-day OLR anomalies over the tropical western Pacific and Indian Ocean (5°–25°N, 50°–130°E; red frame in Fig. 6e) during the TC season are larger/smaller than one standard deviation. Figure 13 compares the TC activities during AWB with and without the tropical convection signals. Without the impact of tropical convection, the influences of AWB on TC activities are still clear (right-hand panels of Fig. 13) and consistent with the earlier findings based on all AWBs (left-hand panels of Fig. 13). In other words, the AWB itself may drive the large-scale changes to reduce the TC frequency and ACE over the open ocean of the WNP, regardless of the strength of the tropical convection anomalies (Figs. 13b,c). Similar results are derived when we focus on a smaller domain of the tropical convection signal over the SCS (100°–130°E, 5°–25°N; not shown). MacRitchie and Roundy (2016) documented that the MJO convection over the tropical Indian Ocean could induce AWB over the North Pacific. This suggests that the intensity of AWB may be impacted by the tropical convection.

To quantify the relative effects of AWBs and tropical convection on TC activity, we calculated the partial correlations between the TC activity metrics (including genesis number, frequency, and ACE) over different basins and AWBisv/the tropical intraseasonal convection index (Table 1). Although the AWBisv is significantly correlated with tropical convection index (with a coefficient of −0.24), as also discussed in Fig. 6, they show distinct influences on WNP TC activity. The statistically significant partial correlations between AWBisv and the TC frequency and ACE also indicate a robust AWB modulation of TC activities at subseasonal time scales. In addition, we found that the tropical

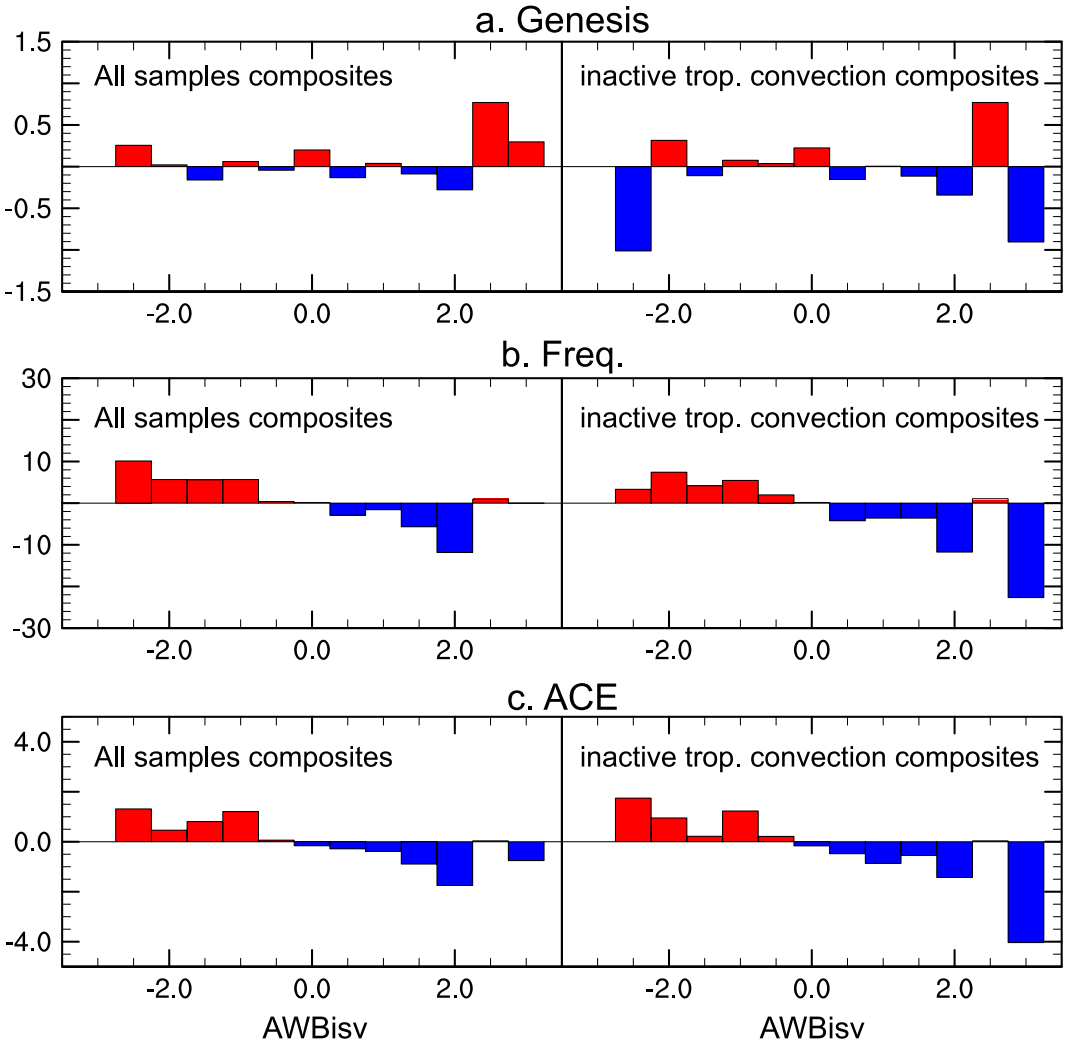

FIG. 13. Changes in the (a) TC genesis number, (b) TC frequency, and (c) ACE (10^4 m^2 s^{-2}) associated with phases of the AWBisv index (x axis). (left) Composites for all AWBisv samples (total: 756 samples = 18 × 42 years) and (right) the results for samples with inactive tropical convection (534 samples).

intraseasonal convection can induce a favorable environment, which significantly increases the TC genesis number, frequency, and ACE, but only over the SCS; it shows little influence on the TC activities over the WNP open ocean.

5. Summary and discussion

Subseasonal TC predictions are still challenging because of a limited understanding of the sources of subseasonal predictability (Camargo et al. 2019; Lee et al. 2020). Previous studies

TABLE 1. Partial correlations between AWBisv (tropical convection index) and TC activities over the open ocean of the WNP and the SCS. One and two asterisks denote that the partial correlation is significant at the 95% and 99% confidence levels based on the effective degrees of freedom, respectively.

Partial correlations between the left and right columns		Open ocean (12.5°–37.5°N, 127.5°–172.5°E)	SCS (12.5°–20°N, 100°–127.5°E)
AWBisv	TC genesis	−0.05	0.07
	TC frequency	−0.25**	0.10*
	ACE	−0.19**	0.12*
Tropical intraseasonal convection index	TC genesis	0.01	−0.14*
	TC frequency	0.07	−0.18**
	ACE	0.08	−0.15*

have focused on the effects of tropical intraseasonal oscillations on WNP TC activity (Zhao et al. 2015). The manner and extent to which the extratropical variability at subseasonal time scales influences WNP TC activities are rarely discussed. The aim in this study was to unveil the intraseasonal variations of AWB and their effects on TC activity over the WNP.

Though AWB itself is a synoptic-scale feature occurring in midlatitude regions (Figs. 1 and 2), we found that the frequency of AWB occurrence over the North Pacific shows significant variability at subseasonal time scales (7–40 days, Fig. 3). The intraseasonal AWB signal over the North Pacific is related to upstream Rossby wave activity and local anomalies in the jet stream strength. A Rossby wave train structure across Eurasia becomes clear around 12 days before AWB, which is enhanced and propagates eastward toward northern Asia and the western-central North Pacific (Fig. 5b). When the zonal winds weaken at the exit region over the North Pacific, AWB is accompanied by an equatorward WAF (Fig. 6).

Increased AWB occurrence is associated with decreased ACE over the WNP open ocean and increased ACE over the SCS (Fig. 8). We further found that the changes in ACE induced by AWB result from AWB modulations of the TC count, average duration, and average intensity through anomalous large-scale conditions (Fig. 9). For example, anticyclonic circulation, a dry and cold troposphere, increased VWS, and descending motion prevail over the open ocean of the WNP when AWB occurs. On the other hand, cyclonic circulation, ascending motion, and enhanced convection in the southwestern quadrant of AWB favor vigorous TC activities over the SCS (Figs. 10–12). These mechanisms responsible for the AWB-induced WNP TC activity changes on intraseasonal time scales are generally consistent with the results of previous studies that focused either on the AWB–TC relationship on interannual time scales (Zhang et al. 2016, 2017; Bian et al. 2018) or over different basins (Li et al. 2018).

The major findings of this study highlight the intraseasonal modulation by an extratropical system (AWB) of the tropical TC activity over the WNP, which provides the opportunity to use AWB as a source of subseasonal TC predictability (Camargo et al. 2019). To highlight the significance of the role played by AWBs in subseasonal WNP TC activities, we also compared the TC variations with and without the joint effects of the tropical intraseasonal anomalies (Fig. 13). The results showed that the AWB-induced TC activity anomalies remain consistent during AWBs without the tropical convection signals. Recent but limited studies have supported the impact of AWBs on Atlantic TC predictability. By assessing the reforecast data of the Global Ensemble Forecasting System, Li et al. (2018) showed that the predictive skill for Atlantic TCs is reduced during years of enhanced AWB activity. Papin et al. (2023) also found that overestimated AWB frequency in the Navy Earth System Prediction Capability 45-day forecast corresponds to an underestimated prediction of TC activities at subseasonal time scales over the North Atlantic. Our ongoing research will focus on whether North Pacific AWB is a useful signal for improving subseasonal TC predictions.

Another unsolved issue is the origins of intraseasonal AWB variability over the North Pacific. Although intraseasonal AWB was found to be associated with the Rossby wave train across Eurasia with an amplified wave train and eastward WAF in the current study, the potential downstream effect needs to be further verified since the activities of AWB over the North Pacific and North Atlantic might interact with each other. For example, Benedict et al. (2004) suggested that AWB over the North Atlantic is associated with upstream AWB over the North Pacific and revealed the role of AWBs in the phase transition and maintenance of the North Atlantic Oscillation (NAO), but whether and to what extent AWB over the North Atlantic and the NAO influence the activities of AWB over the North Pacific is still uncertain. Aside from the upstream signals from the North Atlantic, the Silk Road teleconnection pattern along the westerly jet may also induce the occurrence of AWB over the North Pacific (Takemura and Mukougawa 2020a). Apart from these downstream effects, local effects may also contribute to the variance of AWB. Zhang and Wang (2018) suggested that the local diabatic heating processes near the AWB region play a vital role in contributing to the rapid amplification of the anomalous anticyclone associated with AWB over the North Atlantic based on diagnostic results of a PV budget analysis. The relative effects of upstream and local signals on the occurrence of intraseasonal AWB variability over the North Pacific will be investigated in our group's future work.

Acknowledgments. We appreciate the valuable comments and suggestions from the editor and anonymous reviewers, which significantly improved the manuscript. The authors also thank Dr. Nathaniel Johnson for his valuable suggestions. This work was supported by the National Natural Science Foundation of China (42205024), the National Postdoctoral Program for Innovative Talent (BX2021133), the China Postdoctoral Science Foundation of No. 70 General Fund (2021M701753), and the Natural Science Foundation of Jiangsu Province, China (BK20220459). We acknowledge the High-Performance Computing Center of Nanjing University of Information Science and Technology for their support of this work.

Data availability statement. ERA5 data can be acquired from the ECMWF website at https://apps.ecmwf.int/datasets/ and https://www.ecmwf.int/en/forecasts/datasets/reanalysis-datasets/era5. The NOAA daily OLR data can be found at https://psl.noaa.gov/data/gridded/data.uninterp_OLR.html. The Regional Specialized Meteorological Center (RSMC) Tokyo–Typhoon Center best track dataset is available at https://www.jma.go.jp/jma/jma-eng/jma-center/rsmc-hp-pub-eg/trackarchives.html. The U.S. Department of Defense Joint Typhoon Warning Center Best Track Database is available at https://www.metoc.navy.mil/jtwc/jtwc.html?western-pacific.

REFERENCES

Abatzoglou, J. T., and G. Magnusdottir, 2006: Planetary wave breaking and nonlinear reflection: Seasonal cycle and interannual variability. *J. Climate*, **19**, 6139–6152, https://doi.org/10.1175/JCLI3968.1.

Aemisegger, F., and Coauthors, 2021: How Rossby wave breaking modulates the water cycle in the North Atlantic trade wind

region. *Wea. Climate Dyn.*, **2**, 281–309, https://doi.org/10.5194/wcd-2-281-2021.

Appenzeller, C., and H. C. Davies, 1992: Structure of stratospheric intrusions into the troposphere. *Nature*, **358**, 570–572, https://doi.org/10.1038/358570a0.

Atkinson, G. D., 1974: Investigation of gust factors in tropical cyclones. Fleet Weather Central/Joint Typhoon Warning Center Tech. Note. FLEWEACEN/JTWC-TN-74-1, 15 pp., https://apps.dtic.mil/dtic/tr/fulltext/u2/a064535.pdf.

Bell, G. D., and Coauthors, 2000: Climate assessment for 1999. *Bull. Amer. Meteor. Soc.*, **81** (6), S1–S50, https://doi.org/10.1175/1520-0477(2000)81[s1:CAF]2.0.CO;2.

Benedict, J. J., S. Lee, and S. B. Feldstein, 2004: Synoptic view of the North Atlantic Oscillation. *J. Atmos. Sci.*, **61**, 121–144, https://doi.org/10.1175/1520-0469(2004)061<0121:SVOTNA>2.0.CO;2.

Bian, J., J. Fang, G. Chen, and C. Liu, 2018: Circulation features associated with the record-breaking typhoon silence in August 2014. *Adv. Atmos. Sci.*, **35**, 1321–1336, https://doi.org/10.1007/s00376-018-7294-4.

Bowley, K. A., J. R. Gyakum, and E. H. Atallah, 2019: A new perspective toward cataloging Northern Hemisphere Rossby wave breaking on the dynamic tropopause. *Mon. Wea. Rev.*, **147**, 409–431, https://doi.org/10.1175/MWR-D-18-0131.1.

Camargo, S. J., and Coauthors, 2019: Tropical cyclone prediction on subseasonal time-scales. *Trop. Cyclone Res. Rev.*, **8**, 150–165, https://doi.org/10.1016/j.tcrr.2019.10.004.

Drews, C., 2007: Separating the ACE hurricane index into number, intensity, and duration. Accessed 24 August 2007, https://acomstaff.acom.ucar.edu/drews/hurricane/SeparatingTheACE.html.

Feng, X., and L. Wu, 2022: Roles of interdecadal variability of the western North Pacific monsoon trough in shifting tropical cyclone formation. *Climate Dyn.*, **58**, 87–95, https://doi.org/10.1007/s00382-021-05891-w.

Franzke, C., S. B. Feldstein, and S. Lee, 2011: Synoptic analysis of the Pacific–North American teleconnection pattern. *Quart. J. Roy. Meteor. Soc.*, **137**, 329–346, https://doi.org/10.1002/qj.768.

Ghil, M., and Coauthors, 2002: Advanced spectral methods for climatic time series. *Rev. Geophys.*, **40**, 1003, https://doi.org/10.1029/2000RG000092.

Hersbach, H., and Coauthors, 2018: ERA5 hourly data on single levels from 1979 to present. Copernicus Climate Change Service (C3S) Climate Data Store (CDS), accessed 1 June 2021, https://cds.climate.copernicus.eu/cdsapp#!/dataset/reanalysis-era5-single-levels?tab=overview.

——, and Coauthors, 2020: The ERA5 global reanalysis. *Quart. J. Roy. Meteor. Soc.*, **146**, 1999–2049, https://doi.org/10.1002/qj.3803.

Hu, H., F. Dominguez, Z. Wang, D. A. Lavers, G. Zhang, and F. M. Ralph, 2017: Linking atmospheric river hydrological impacts on the U.S. West Coast to Rossby wave breaking. *J. Climate*, **30**, 3381–3399, https://doi.org/10.1175/JCLI-D-16-0386.1.

Jones, J. J., M. M. Bell, P. J. Klotzbach, and E. A. Barnes, 2022: Wintertime Rossby wave breaking persistence in extended-range seasonal forecasts of Atlantic tropical cyclone activity. *J. Climate*, **35**, 2133–2147, https://doi.org/10.1175/JCLI-D-21-0213.1.

Lee, C.-Y., S. J. Camargo, F. Vitart, A. H. Sobel, J. Camp, S. Wang, M. K. Tippett, and Q. Yang, 2020: Subseasonal predictions of tropical cyclone occurrence and ACE in the S2S dataset. *Wea. Forecasting*, **35**, 921–938, https://doi.org/10.1175/WAF-D-19-0217.1.

Li, W., Z. Wang, G. Zhang, M. S. Peng, S. G. Benjamin, and M. Zhao, 2018: Subseasonal variability of Rossby wave breaking and impacts on tropical cyclones during the North Atlantic warm season. *J. Climate*, **31**, 9679–9695, https://doi.org/10.1175/JCLI-D-17-0880.1.

Liebmann, B., and C. A. Smith, 1996: Description of a complete (interpolated) outgoing longwave radiation dataset. *Bull. Amer. Meteor. Soc.*, **77**, 1275–1277, https://doi.org/10.1175/1520-0477-77.6.1274.

MacRitchie, K., and P. E. Roundy, 2016: The two-way relationship between the Madden–Julian oscillation and anticyclonic wave breaking. *Quart. J. Roy. Meteor. Soc.*, **142**, 2159–2167, https://doi.org/10.1002/qj.2809.

McIntyre, M. E., and T. N. Palmer, 1983: Breaking planetary waves in the stratosphere. *Nature*, **305**, 593–600, https://doi.org/10.1038/305593a0.

Messori, G., and R. Caballero, 2015: On double Rossby wave breaking in the North Atlantic. *J. Geophys. Res. Atmos.*, **120**, 11 129–11 150, https://doi.org/10.1002/2015JD023854.

Moore, B. J., D. Keyser, and L. F. Bosart, 2019: Linkages between extreme precipitation events in the central and eastern United States and Rossby wave breaking. *Mon. Wea. Rev.*, **147**, 3327–3349, https://doi.org/10.1175/MWR-D-19-0047.1.

Papin, P. P., C. A. Reynolds, and M. A. Janiga, 2023: Linkages between potential vorticity streamer activity and tropical cyclone predictability on subseasonal timescales. *Mon. Wea. Rev.*, **151**, 1005–1017, https://doi.org/10.1175/MWR-D-22-0038.1.

Polvani, L. M., and J. G. Esler, 2007: Transport and mixing of chemical air masses in idealized baroclinic life cycles. *J. Geophys. Res.*, **112**, D23102, https://doi.org/10.1029/2007JD008555.

Qian, Y., P.-C. Hsu, H. Murakami, B. Xiang, and L. You, 2020: A hybrid dynamical-statistical model for advancing subseasonal tropical cyclone prediction over the western North Pacific. *Geophys. Res. Lett.*, **47**, e2020GL090095, https://doi.org/10.1029/2020GL090095.

Rivière, G., A. Laîné, G. Lapeyre, D. Salas-Mélia, and M. Kageyama, 2010: Links between Rossby wave breaking and the North Atlantic Oscillation–Arctic Oscillation in present-day and last glacial maximum climate simulations. *J. Climate*, **23**, 2987–3008, https://doi.org/10.1175/2010JCLI3372.1.

Samanta, D., M. K. Dash, B. N. Goswami, and P. C. Pandey, 2016: Extratropical anticyclonic Rossby wave breaking and Indian summer monsoon failure. *Climate Dyn.*, **46**, 1547–1562, https://doi.org/10.1007/s00382-015-2661-7.

Song, L., and R. Wu, 2021: Two types of Rossby wave breaking events and their influences on East Asian winter temperature. *J. Geophys. Res. Atmos.*, **126**, e2020JD033917, https://doi.org/10.1029/2020JD033917.

Strong, C., and G. Magnusdottir, 2008: How Rossby wave breaking over the Pacific forces the North Atlantic Oscillation. *Geophys. Res. Lett.*, **35**, L10706, https://doi.org/10.1029/2008GL033578.

Takemura, K., and H. Mukougawa, 2020a: Dynamical relationship between quasi-stationary Rossby wave propagation along the Asian jet and Pacific–Japan pattern in boreal summer. *J. Meteor. Soc. Japan*, **98**, 169–187, https://doi.org/10.2151/jmsj.2020-010.

——, and ——, 2020b: Maintenance mechanism of Rossby wave breaking and Pacific–Japan pattern in boreal summer. *J. Meteor. Soc. Japan*, **98**, 1183–1206, https://doi.org/10.2151/jmsj.2020-061.

——, and ——, 2021: Tropical cyclogenesis triggered by Rossby wave breaking over the western North Pacific. *SOLA*, **17**, 164–169, https://doi.org/10.2151/sola.2021-029.

——, ——, and S. Maeda, 2020: Large-scale atmospheric circulation related to frequent Rossby wave breaking near Japan in boreal summer. *J. Climate*, **33**, 6731–6744, https://doi.org/10.1175/JCLI-D-19-0958.1.

Takaya, K., and H. Nakamura, 2001: A formulation of a phase-independent wave-activity flux for stationary and migratory quasi-geostrophic eddies on a zonally varying basic flow. *J. Atmos. Sci.*, **58**, 608–627, https://doi.org/10.1175/1520-0469(2001)058<0608:AFOAPI>2.0.CO;2.

Thorncroft, C. D., B. J. Hoskins, and M. E. McIntyre, 1993: Two paradigms of baroclinic-wave life-cycle behavior. *Quart. J. Roy. Meteor. Soc.*, **119A**, 17–55, https://doi.org/10.1002/qj.49711950903.

Wang, C., and L. Wu, 2016: Interannual shift of the tropical upper-tropospheric trough and its influence on tropical cyclone formation over the western North Pacific. *J. Climate*, **29**, 4203–4211, https://doi.org/10.1175/JCLI-D-15-0653.1.

Wang, X., W. Randel, L. Pan, Y. Wu, and P. Zhang, 2022: Transient behavior of the Asian summer monsoon anticyclone associated with eastward eddy shedding. *J. Geophys. Res. Atmos.*, **127**, e2021JD036090, https://doi.org/10.1029/2021JD036090.

Wang, Z., G. Zhang, T. J. Dunkerton, and F.-F. Jin, 2020: Summertime stationary waves integrate tropical and extratropical impacts on tropical cyclone activity. *Proc. Natl. Acad. Sci. USA*, **117**, 22 720–22 726, https://doi.org/10.1073/pnas.2010547117.

Waugh, D. W., and L. M. Polvani, 2000: Climatology of intrusions into the tropical upper troposphere. *Geophys. Res. Lett.*, **27**, 3857–3860, https://doi.org/10.1029/2000GL012250.

——, and Coauthors, 1994: Transport out of the lower stratospheric Arctic vortex by Rossby wave breaking. *J. Geophys. Res.*, **99**, 1071–1088, https://doi.org/10.1029/93JD02556.

Wernli, H., and M. Sprenger, 2007: Identification and ERA-15 climatology of potential vorticity streamers and cutoffs near the extratropical tropopause. *J. Atmos. Sci.*, **64**, 1569–1586, https://doi.org/10.1175/JAS3912.1.

Woollings, T., B. Hoskins, M. Blackburn, and P. Berrisford, 2008: A new Rossby wave–breaking interpretation of the North Atlantic Oscillation. *J. Atmos. Sci.*, **65**, 609–626, https://doi.org/10.1175/2007JAS2347.1.

——, J. G. Pinto, and J. A. Santos, 2011: Dynamical evolution of North Atlantic ridges and poleward jet stream displacements. *J. Atmos. Sci.*, **68**, 954–963, https://doi.org/10.1175/2011JAS3661.1.

Wu, L., C. Wang, and B. Wang, 2015: Westward shift of western North Pacific tropical cyclogenesis. *Geophys. Res. Lett.*, **42**, 1537–1542, https://doi.org/10.1002/2015GL063450.

Zavadoff, B. L., and B. P. Kirtman, 2021: The Pacific decadal oscillation as a modulator of summertime North Atlantic Rossby wave breaking. *Climate Dyn.*, **56**, 207–225, https://doi.org/10.1007/s00382-020-05475-0.

Zhang, G., and Z. Wang, 2018: North Atlantic extratropical Rossby wave breaking during the warm season: Wave life cycle and role of diabatic heating. *Mon. Wea. Rev.*, **146**, 695–712, https://doi.org/10.1175/MWR-D-17-0204.1.

——, ——, T. J. Dunkerton, M. S. Peng, and G. Magnusdottir, 2016: Extratropical impacts on Atlantic tropical cyclone activity. *J. Atmos. Sci.*, **73**, 1401–1418, https://doi.org/10.1175/JAS-D-15-0154.1.

——, ——, M. S. Peng, and G. Magnusdottir, 2017: Characteristics and impacts of extratropical Rossby wave breaking during the Atlantic hurricane season. *J. Climate*, **30**, 2363–2379, https://doi.org/10.1175/JCLI-D-16-0425.1.

——, and Coauthors, 2021: Seasonal predictability of baroclinic wave activity. *npj Climate Atmos. Sci.*, **4**, 50, https://doi.org/10.1038/s41612-021-00209-3.

Zhao, H., X. Jiang, and L. Wu, 2015: Modulation of Northwest Pacific tropical cyclone genesis by the intraseasonal variability. *J. Meteor. Soc. Japan*, **93**, 81–97, https://doi.org/10.2151/jmsj.2015-006.